AN AXIALLY EXTRACTED VIRTUAL CATHODE OSCILLATOR DESIGN AND CHARACTERIZATION

A THESIS SUBMITTED TO
THE GRADUATE SCHOOL OF NATURAL AND APPLIED SCIENCES
OF
MIDDLE EAST TECHNICAL UNIVERSITY

BY

BÜŞRA TİMUR

IN PARTIAL FULFILLMENT OF THE REQUIREMENTS
FOR
THE DEGREE OF MASTER OF SCIENCE
IN
ELECTRICAL AND ELECTRONICS ENGINEERING

SEPTEMBER 2018

Approval of the thesis:

AN AXIALLY EXTRACTED VIRTUAL CATHODE OSCILLATOR DESIGN AND CHARACTERIZATION

submitted by **BÜŞRA TİMUR** in partial fulfillment of the requirements for the degree of **Master of Science in Electrical and Electronics Engineering Department, Middle East Technical University** by,

Prof. Dr. Halil Kalıpçılar _____
Dean, Graduate School of **Natural and Applied Sciences**

Prof. Dr. Tolga Çiloğlu _____
Head of Department, **Electrical and Electronics Engineering**

Prof. Dr. Şimşek Demir _____
Supervisor, **Electrical and Electronics Eng. Dept., METU**

Examining Committee Members:

Prof. Dr. Sencer Koç
Electrical and Electronics Eng. Dept., METU _____

Prof. Dr. Şimşek Demir
Electrical and Electronics Eng. Dept., METU _____

Assoc. Prof. Dr. Lale Alatan
Electrical and Electronics Eng. Dept., METU _____

Assoc. Prof. Dr. Serhat Çakır
Physics Dept., METU _____

Prof. Dr. Asım Egemen Yılmaz
Electrical and Electronics Eng. Dept., Ankara University _____

Date: _____

I hereby declare that all information in this document has been obtained and presented in accordance with academic rules and ethical conduct. I also declare that, as required by these rules and conduct, I have fully cited and referenced all material and results that are not original to this work.

Name, Last Name: BÜŞRA TİMUR

Signature :

ABSTRACT

AN AXIALLY EXTRACTED VIRTUAL CATHODE OSCILLATOR DESIGN AND CHARACTERIZATION

Timur, Büşra
M.S., Department of Electrical and Electronics Engineering
Supervisor : Prof. Dr. Şimşek Demir

September 2018, 92 pages

This thesis investigates axially extracted virtual cathode oscillator, which is one of the HPM sources, in several aspects. First, the cathode ring structure is defined, and effects of that structure are interpreted. Besides, the dependency between current density characteristics in the diode region of the studied vircator and the defined power conversion efficiency is shown. Moreover, the input characteristic of the vircator is examined in terms of the applied inlet voltage and corresponding inlet current. By taking these waveforms into consideration, the input port of the vircator is modeled with an equivalent electric circuit. Then, the variation of the modeled electric circuit component values with respect to the vircator's design parameters is analyzed.

Keywords: HPM, Vircator, Virtual Cathode, Space-Charge Limiting Current

ÖZ

EKSENEL ÇIKARTILMIŞ SANAL KATOT OSİLATÖR TASARIMI VE KARAKTERİZASYONU

Timur, Büşra
Yüksek Lisans, Elektrik ve Elektronik Mühendisliği Bölümü
Tez Yöneticisi : Prof. Dr. Şimşek Demir

Eylül 2018 , 92 sayfa

Bu tez YGM kaynaklarından biri olan eksenel çıkartılmış sanal katot osilatörünü çeşitli açılardan incelemiştir. İlk olarak, katot halka yapısı tanımlandı ve bu yapının etkileri yorumlanmıştır. Ayrıca, çalışılan bu virkatörün diyot bölgesindeki akım yoğunluğu karakteri ile tanımlanıp güç dönüşüm verimi arasındaki ilşki gösterilmiştir. Bunlara ek olarak, virkatörün giriş karakteristiği uygulanan giriş voltajı ve buna karşılık gelen giriş akımı cinsinden irdelenmiştir. Bu dalga formları dikkate alınarak, virkatörün giriş portunun eşdeğer elektrik devresi modellenmiştir. Daha sonra, modellenen elektrik devresi bileşenlerinin sayısal değerlerinin virkatörün tasarım parametrelerine göre değişimi incelenmiştir.

Anahtar Kelimeler: YGM, Virkatör, Sanal Katot, Uzay-Yük Sınırlama Akımı

To my family...

ACKNOWLEDGMENTS

This thesis work would not have become a reality without the kind support and help of many individuals. I would like to extend my sincere thanks to all of them.

Foremost, I owe my deepest gratitude to Prof. Dr. Şimşek Demir, my thesis advisor, for his expertise, guidance, and valuable comments. He has provided me the benefits of his own numerical experience. It is a great honor to work under his supervision.

I also would like to express my gratitude to Zafer Tanç for his academic supervision and personal support throughout all the time worked together, and even broad perspective that I gained not only for this thesis work but also as being an engineer thanks to him.

I would like to thank my esteemed colleague İbrahim Semih Küçük for his effort, collaboration, contribution and help since the very beginning of the whole master period.

My thankfulness is also for members of ARC304. I would like to thank Enis Kobal and Cihan Aşcı for their support and friendship during the times we share the same office.

I will always be grateful to my dearest friends Merve Acar, Melike Bayana, Ayça Bayram, Hüseyin Boyacı, Selva Sargın Güçlü, Seren Oğuz, Özge Önceler, Elif Aksu Taşdelen and Berk Yaşyerli for not letting me give up. They are like a second family to me.

I would also like to say a heartfelt thank to Mustafa Üstündağ, Şükran Üstündağ, Reyhan Üstündağ Dirim and Murat Dirim for always believing in me. Their support is unparalleled for me.

I take this opportunity to record my unique and profound gratitude to my family. I cannot express enough thank to my mother Emine Timur, my father Mahmut Timur,

my grandmother Fatma Koçak for giving me this life, thank you for your everlasting love and supports, your lifetime sacrifices, patients and encourages. Without you, none of this work would indeed be possible. I would especially like to thank my sister Beyza Timur, my cousin Mustafa Selim Koçak and my uncle Ersin Koçak. It would be impossible to imagine myself in my current position without their support and encouragement.

Last but not least, I would like to show my deepest gratitude to my fiancé Oğuzhan Üstündağ for his everlasting love, patience, precious support, and endless encouragement.

Büşra TİMUR

TABLE OF CONTENTS

LIST OF TABLES

TABLES

LIST OF FIGURES

FIGURES

LIST OF ABBREVIATIONS

1D	1 Dimensional
2D	2 Dimensional
3D	3 Dimensional
AK Gap	Anode Cathode Gap
BWO	Backward Wave Oscillator
CEA	Le Commissariat à l'énergie atomique et aux énergies alternatives
CFA	Cross-Field Amplifier
CL	Child-Langmuir
E field	Electrical Field
FDTD	Finite Difference Time Domain
FFT	Fast Fourier Transform
H field	Magnetic Field
HPM	High Power Microwave
IHCE	Institute of High Current Electronics
KIPT	Kharkiv Institute of Physics and Technology
KU	Kwangwoon University
LANL	Los Alamos National Laboratory
LLNL	Lawrence Livermore National Laboratory
NRL	Naval Research Laboratory
NUDT	National University of Defence Technology
PIC	Particle-In-Cell
TE	Transverse Electric
TM	Transverse Magnetic

TTU	Texas Technical University
TWT	Traveling Wave Tube
Vircator	VIRtual CAThode oscillaTOR
VC	Virtual Cathode
YGM	Yüksek Güçlü Mikrodalga

CHAPTER 1

INTRODUCTION

The first conventional microwave vacuum tube which is named as klystron was invented in 1937 [1, 2]. Along with World War II, vacuum tube devices made a breakthrough, and important types of them, which are a magnetron, a traveling wave tube (TWT) and a backward wave oscillator (BWO) were developed. These devices were an old generation of high power microwave tubes. Later, a crossed-field amplifier (CFA) was improved. After the invention of semiconductor devices, conventional microwave vacuum tubes lost their popularity and replaced with solid-state based devices. It is because latter devices offer more durable, efficient and reliable operation with a smaller size. However, solid-state based devices are not capable of handling high power due to its nature and size. With the aid of comprehension of the interaction between particles and waves by nuclear fusion research, intense electron beam technologies were promoted at the same time. In line with these developments, vacuum tube devices got ahead in a generation of a high power microwave. HPM sources transfer the energy of the electron to the microwave by employing intense electron beam in order to achieve high power output [3]. It is crucial to use such a short pulse duration that HPM sources properly operate without experiencing pulse shortening phenomena.

As a well-known type of space charge devices, which is a subclass of the HPM sources, virtual cathode oscillator (vircator) generates microwave power by forming a virtual cathode in a drift tube [1]. The virtual cathode formation is achieved by an injection of the electron beam into the drift tube whose space-charge limiting current is exceeded by the beam current. Based on this phenomena, many research groups have conducted several studies on it since the invention time of the vircator. These

efforts vary regarding an understanding of microwave generation mechanism, analyzing a frequency spectrum of the vircator, identifying mode characteristics of the output field. At the bottom, almost all studies focus on enhancing the power conversion efficiency of the vircator. For this purpose, more complicated vircator structures are also proposed. Even though each structure are based upon the same phenomena, it is required an individual effort in order to digest them in every aspect. The axial vircator is one of the most basic types of the vircator. However, many groups have still studied it because it is the essential one to comprehend the operation fundamentals of the vircator such that other types of it can be easily followed.

In this thesis work, it is aimed to investigate the axial vircator in three main aspects. First, effects of the space charge limiting current are examined. Second, effects of a definition of a cathode ring are discussed regarding the emitted current and the efficiency. Furthermore, mode analysis of the axial vircator is performed. Last, characterization of the input port of the axial vircator is proposed. All simulations within the scope of this thesis work are utilized via Magic simulation software. Magic simulation program is based on FDTD and EM PIC methods, together. It differs from the commercial electromagnetic wave simulation programs such as CST and HFSS regarding involving physics of particles. Hence, it is also learned how to use Magic 3D in order to perform reliable simulations effectively.

This thesis composes of six main chapters with the introduction and a conclusion. In the first chapter after the introduction, the basic physical concepts related to the operation of the vircator are introduced. Moreover, a brief history of the vircator is given in this chapter, as well. In the third chapter, An overview regarding 3D Magic simulation program is given. Then, arrangements for the simulation setup are explained, in detail. In the fourth chapter, the effect of defining cathode ring is discussed. Moreover, a behavior of the emitting current of the axial vircator by varying several parameters of the axial vircator such as an AK gap separation, a radius of the cathode and an applied voltage difference is examined by taking the space charge limiting current into the consideration. In addition to that, a variation of the axial vircator efficiency is evaluated for the space charge limiting current, as well. Furthermore, output field modes of the axial vircator are identified, as well. In the fifth chapter, an electrical model of the input port of the axial vircator is suggested.

A deviation on the components' values of the proposed model for parameters of the axial vircator are also investigated. In the last chapter, the results of the thesis are summarized as a conclusion.

In this thesis, it is aimed to show the effects of the space charge limiting current on both the emitting current and the efficiency of the axial vircator. Furthermore, an electrical circuit model for the input port of the axial vircator is suggested. Then, a variation of its components' values with respect to parameters of the axial vircator is investigated.

CHAPTER 2

A REVIEW OF THE VIRCATOR

The vircator is one of the well-known vacuum tube oscillators. It is capable to output power in the order of GW in sub-microsecond pulse length at frequencies in the range of 1-10 GHz[1]. It does not require any external magnetic field to generate microwave, so it is robust and simple to build as compared with other microwave tubes. Moreover, the vircator gives an opportunity to broad frequency tunability.

On the contrary, it is at a disadvantage of low power conversion efficiency, which is typically well below 10% for the recognized structures listed in [1]. Thus, in general, all effort regarding the vircator is to enhance the efficiency of the vircator. The other drawback of the vircator is gap closure, which is detailedly discussed in Section 2.3.1.

2.1 Historical Development of Vircator

In the 1910s, the limit for the charged particle beam flow in a planar diode was claimed by Child and Langmuir [4, 5]. After a long time from the date of the revealing of Child-Langmuir (CL) law, in 1966, Birdsall and Bridges discovered the formation of the virtual cathode in the case of excessing space-charge limiting current. In 1977, researchers at NRL were the first to generate microwave power experimentally due to the reflexing electrons from virtual cathode [6]. Reflex triode structure was performed during the experiment. Then, in 1979, Sullivan stated that the oscillation of virtual cathode itself is responsible for microwave production [7]. This result was obtained in a simulation environment. Moreover, in [3], it is reported that the first published results for the axial vircator structure belong to Buzzi and coworkers [8]. Then, to improve the efficiency of the vircator, some modifications are made. In 1987, the

cavity vircator was proposed by Benford and coworkers. The formed virtual cathode was enclosed with a circular cylinder. It was reported that efficiency is enhanced four times by the cavity's forcing oscillation at only desired frequency and eliminating others [9]. Later, the reditron was established by the researcher at Los Alamos National Laboratory (LANL) in 1988. In this structure, an axial magnetic field was used to align the electron beam to pass through the slotted anode. By this way, it is aimed to prevent the effect of the reflexing electrons, and 3.5 factor efficiency enhancement was reported [10]. In 1991, the double anode was introduced at Lawrence Livermore National Laboratory (LLNL). It was presented that the frequency components of both virtual cathode oscillation and reflexing electrons are equalized by defining a delay for the reflexing electrons[11]. In 1993, the virtode was developed at Kharkiv Institute of Physics and Technology (KIPT). The main idea of the structure is to feedback the diode region with the generated microwave. In [1], it was noted that the efficiency of the virtode could be changed between 3% and 17% with the frequency spectrum which ranged from the S-band to X-band. Then, in 1997, the most popular and studied structure, which is the coaxial vircator was described at Texas Technical University (TTU) [12]. After the publication of simulation results, about 2.2 efficiency enhancement was notified in 2000 [13]. In 2002, a new configuration which is a combination of the virtode and the double anode vircator was built at Institute of High Current Electronics (IHCE). 5% power efficiency was experimentally stated in [14]. In 2006, another novel design was implemented at Kwangwoon University (KU) by adding a thick bar reflector located in the drift tube of the coaxial vircator. It was observed that 1.6 factor efficiency increment [15]. In 2008, axial vircator was modified by adding three resonant cavities in the drift region at National University of Defence Technology (NUDT). Insertion of cavities resulted with 6.6% efficiency [16]. In 2016, axial vircator was redesigned at Le Commissariat à l'énergie atomique et aux énergies alternatives (CEA) by adding five reflectors to multiply formation of virtual cathodes, and so increase the beam-field interaction. With this configuration, 21% efficiency was obtained [17].

2.2 Operation Fundamentals

The vircator is simply composed of a diode, which is the source of an electron beam and a drift tube to guide the generated microwave in the desired mode and frequency. When the high voltage is applied to the cathode, the semi-transparent anode is grounded. The regions of the vircator can be seen in Figure 2.1. In the figure, a distance between the cathode and the anode is denoted as d_{AK} which refers to the diode region. On the other hand, a distance between the anode and the virtual cathode is given as $d_{AK}^{'}$, which is in the drift tube region. Due to the existence of the high voltage, the explosive emission process occurs, which is detailedly explained in the next section. The emitted electron from the vicinity of the cathode is accelerated towards the anode with the effect of the E field in the diode region and some of the electrons pass through the anode into the drift tube. If the injected electron beam current, I_b into the drift tube exceeds the space-charge limiting current, I_{SCL} of the drift tube, some part of the electron slow down and turn back to the diode region [1, 3, 18]. Thus, the reflection plane can be defined as a virtual cathode, whose potential is about $-V_0$ [19]. The distance $d_{AK}^{'}$ is also almost the same as the distance d_{AK} [1, 20, 21, 22].

The microwave generation of the vircator is based on the formation of the virtual cathode. Thanks to the presence of the virtual cathode, the reflex electrons are caught in a trap between the real and virtual cathode (VC). The back and forth motion of the reflexing electrons causes a generation of the microwave[6].

After the formation of the virtual cathode, the laminar electron flow cannot be observed anymore, which triggers the virtual cathode to oscillate in time and space [3, 23, 24, 25]. Hence, the oscillation of the virtual cathode itself is also a source of the microwave generation. In both mechanisms of the microwave production, electrons have an accelerated and a decelerated motion, which is known as the Bremsstrahlung radiation (breaking radiation) phenomena [26].

Conceptual sketches of basic vircators are depicted in Figure 2.2. These configurations are based on planar diode structure. The vircators in Figure 2.2a and Figure 2.2b have the negative pulsed cathode and the grounded anode. The only difference between them is the way of extraction. Figure 2.2a shows axially extracted vircator

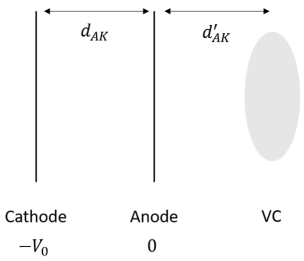

Figure 2.1: Basic schematic of the vircator

whereas, in Figure 2.2b, the side extracted vircator is given. In Figure 2.2c, the reflex triode structure can be seen. It has the grounded cathode and the positive pulsed anode.

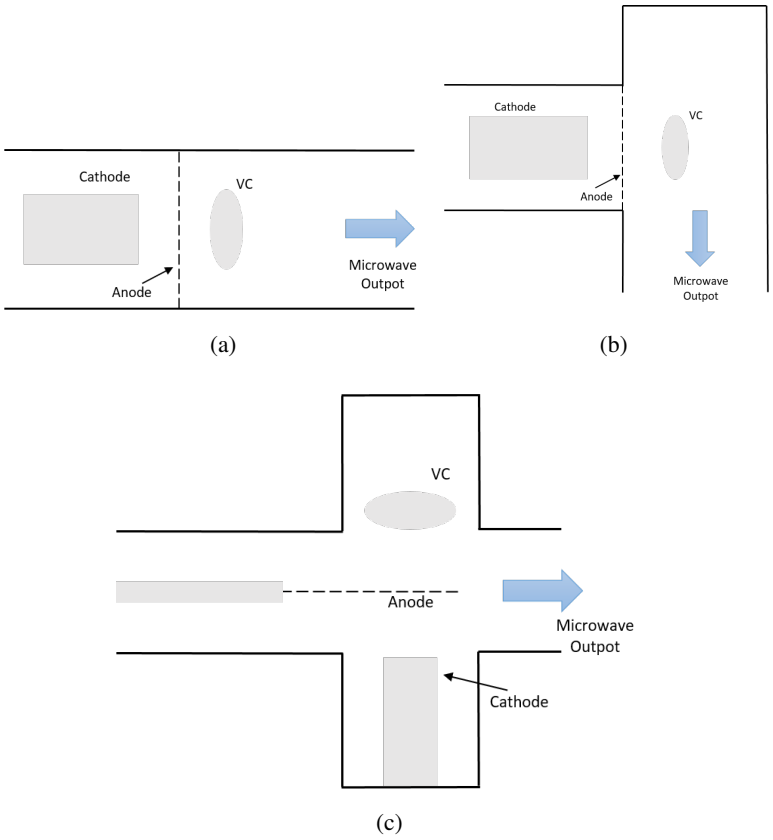

Figure 2.2: Conceptual sketch of (a)axial vircator (b)side extraction (c)reflex triode.

In Figure 2.3, some well-known specialized vircator structures are demonstrated. Figure 2.3a belongs to the coaxial vircator, in which a coaxial diode is used to generate the electron beam. In Figure 2.3b, the double anode vircator is introduced. With

this type of vircator, it is aimed to equate the frequencies of the reflexing electrons and virtual cathode oscillation. In Figure 2.3c, the virtual cathode is enclosed with a resonant cavity to suppress the undesirable frequency components. The reditron can be seen in Figure 2.3d. In this structure, the confined electron beam with the help of external magnetic field passes through the slotted anode, and the effect of the reflex electrons is avoided.

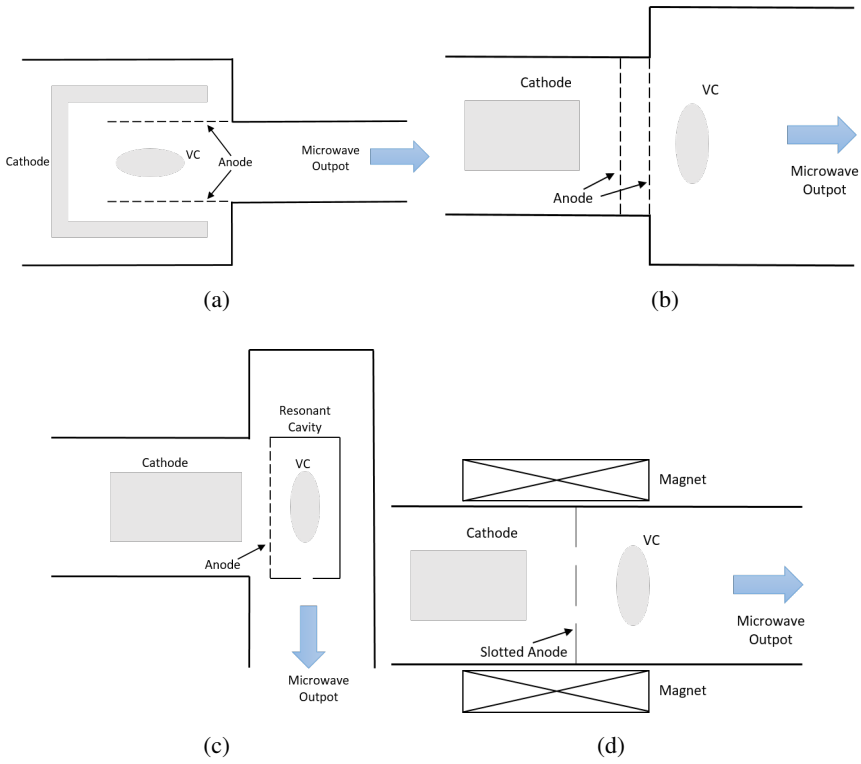

Figure 2.3: Conceptual sketch of (a)coaxial vircator (b)double gap vircator (c)cavity vircator (d)reditron.

2.3 Cold Cathode and Explosive Emission

The cold cathode is the cathode type used in the vircator, to which high voltage in the order of several hundred kV is applied. Due to this high voltage, electron emission can be achieved. The emission process in the cold cathode is explained by the explosive emission mechanism.

Almost any metallic cathode surface contains some surface protrusions in micro-

scopic level due to manufacturing or material itself. In [27], physical dimensions of these surface whiskers are stated as generally on the order of 10^{-4} cm in height and less than 10^{-5} cm base radius. When a high voltage is applied to the cathode, the average electric field on the emitting surface is roughly over 100 kV/cm [1]. However, the electric field at the tips of the microprotrusions is much more enhanced due to the existence of the microprotrusions themselves. Eventually, the enhanced electric field causes Joule heating which triggers explosive evaporation of the whiskers [28, 29, 30]. The evaporated fragments form ionized metallic plasma flares. These flares rapidly start to expand and merge on the surface of the cathode. The composed cathode surface plasma involves unlimited electron, which can generate very high current density up to tens of kA/cm^2 [1]. In other words, for the explosive emission process, cathode surface plasma is the electron source rather than the cathode itself. Another plasma formation during the process of microwave generation from vircator takes place on the anode surface. When the emitted electrons from the cathode plasma pass through the transparent anode, some of them strike the anode and cause the anode heating. Then, anode plasma occurs to emit ions from the anode towards the cathode [30, 31, 32]. This process is called bipolar flow [19, 29].

2.3.1 Effect of Plasma Formation

The plasma which is the source of electron emission has several drawbacks. The most significant disadvantage of the plasma is gap closure. It mainly arises from the expansion of cathode plasma towards the anode and vice versa [29, 33, 34, 35, 36, 37]. Since the plasma can be considered as a conductive surface, plasma expansion over time causes AK gap alteration, which affects space charge limiting current of the diode, a main frequency and also output power of the vircator. Moreover, when the cathode and anode plasma come across into the gap, the gap is short-circuited, and microwave generation ceases. It is called pulse shortening in HPM literature as well [1, 38]. This situation restricts the length of the vircator's input pulse not to cause a reduction in power conversion efficiency of the vircator. In [1] and [19], the maximum length of the pulses for plasma sources is given as 1 ms and 0.5 ms, respectively. These values are consistent with the experimentally found plasma expansion velocities for different cathode type which is typically between 1 and 10 cm/μs

[29, 35, 39, 40].

Another issue related to plasma formation is a lifetime of the cathode. In [1], it is indicated that the explosive emission process and plasma formation do not have any devastating effect on the cathode surface. However, several experimental studies are conducted by several groups and the lifetime for different cathode types are reported [28, 34, 37, 41, 42].

2.4 Space Charge Limiting Current in a Diode

For the classical diode structure, without including the effect of the space charge, a linear potential profile in the diode gap is observed, which can be seen as a blue dash line in Figure 2.4. The constant electric field distribution over the gap is obtained for this case. In the same figure, the green dash line corresponds to zero radial electric field on the cathode surface, and it is the case that the diode reaches its space charge limit. This limitation introduces a space charge limiting current in a diode, which is named as J_{CL}. A further attempt to inject greater current than J_{CL} into the gap causes a negative potential in the vicinity of the cathode. This negative potential avoids further electron emission from the plasma covering the cathode surface [1, 19, 27, 40, 43]. Thus, the electron emission from the plasma, which is considered as an unlimited electron source, is limited by the effect of the electrons' self-space charge.

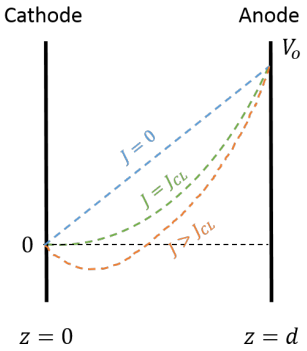

Figure 2.4: Potential profile in a gap for different levels of injected current

2.4.1 Child-Langmuir Law

The Child-Langmuir law gives the maximum steady-state current density J_{CL} which one-dimensional planer diode can carry in a vacuum for specified voltage and gap distance [4, 5]. In the CL law, it is also assumed zero transverse magnetic field and the single species emission with zero initial velocity under non-relativistic case with an electrostatic approach. The ideal Child-Langmuir diode is shown in Figure 2.5. In CL diode, the cathode is located at $z = 0$ with V_0 potential whereas the grounded anode is located at $z = d$.

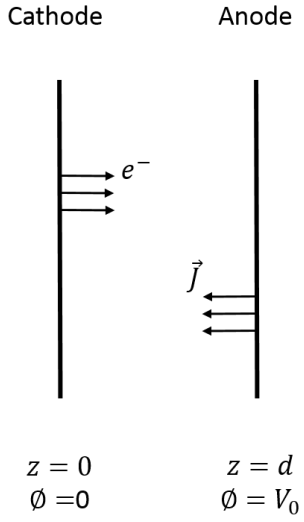

Figure 2.5: Child-Langmuir Diode

In order to derive classical CL current, first 1D current density J in the diode can be written as follows:

$$\vec{J}(z) = J(z)\hat{a}_z = \rho(z)n(z)\hat{a}_z = -en(z)v_z(z)\hat{a}_z \tag{2.1}$$

where e is charge of electron, $n(z)$ is number of electron density and $v_z(z)$ is velocity of an electron. By using the assumption of electrons' leaving the cathode with zero initial velocity under non-relativistic case, the equation for conservation of energy

can be obtained as follow:

$$\frac{1}{2}m_e {v_z}^2 = e\phi(z) \tag{2.2}$$

where m_e is mass of electron and $\phi(z)$ is the electric potential. Moreover, the steady-state condition implies that all physical quantities are time independent. Thus, the Ampere's law in Equation 2.3 can be reduced the form in Equation 2.4 by omitting the first term on the right hand side.

$$\nabla \times \vec{H} = -\frac{\partial \vec{D}}{\partial t} + \vec{J} \tag{2.3}$$

$$\nabla \times \vec{H} = \vec{J} \tag{2.4}$$

By taking the divergence of both sides of the formula in Equation 2.4, $\nabla \cdot \vec{J}$ can be equated to zero due to the null identity, which means that current density, $\vec{J}$ is position independent and can be written as follow:

$$\vec{J}(z) = -env_z\hat{a}_z = -J_{CL}\hat{a}_z \tag{2.5}$$

Then, by substituting Equation 2.2 & Equation 2.5 into the Poisson's equation given in Equation 2.6, differential form of the electric potential can be found as in Equation 2.7.

$$\frac{d^2\phi(z)}{dz^2} = -\frac{\rho(z)}{\epsilon_0} = \frac{en(z)}{\epsilon_0} \tag{2.6}$$

$$\frac{d^2\phi}{dz^2} = -\frac{J_{CL}}{\epsilon_0}\sqrt{\frac{m_e}{2e}}\frac{1}{\phi^{1/2}} \tag{2.7}$$

For simplicity, define $\alpha = -\frac{J_{CL}}{\epsilon_0}\sqrt{\frac{m_e}{2e}}$. Also the boundary conditions for the second order differential equation are $\phi(z=0) = 0$ & $\phi(z=d) = V_0$.

A solution for the electric potential in the gap can be estimated as follows:

$$\phi(z) = V_0\left(\frac{z}{d}\right)^s \tag{2.8}$$

where s is the power of the electric potential, ϕ. Then, by substituting the solution for the electric potential in Equation 2.8 into Equation 2.7, the power of ϕ, s can be found as $\frac{4}{3}$. Thus, the well-known space charge limiting current J_{CL} can be obtained as Equation 2.9

$$J_{CL} = \frac{4\epsilon_0}{9}\sqrt{\frac{2e}{m_e}}\frac{{V_0}^{3/2}}{d^2} \tag{2.9}$$

It is important to note that the formula found in Equation 2.9 is valid only under the assumptions given at the beginning of this section. The non-relativistic condition is satisfied if only applied voltage V_0 is smaller than $500\ kV$ [1, 29, 44].

2.4.2 Multidimensional Extension of 1D CL Law

In [3], it is stated that the emitted current density from a planar diode is defined by the CL relation. However, the derived 1D CL formula is not sufficient to explain the emitted current density for a finite cathode. It is required to add the effect of finite emission surface. For this purpose, the first 2D extension of CL law is introduced by Luginsland et al. [45]. In this study, the uniform electron beam injection from finite strip emitter with width W is applied to the 2D planar diode with gap separation D. For this geometry, two different particle-in-cell (PIC) codes, which are MAGIC and OOPIC, are used, and results are in a good agreement. A resultant plot can be seen in Figure 2.6. In the plot, it can be observed that the normalized 2D CL current approaches to 1 for $W/D >> 1$.

Then, the curve in Figure 2.6, can be fitted with the formula given in Equation 2.10 for $0.1 < W/D < 8$.

$$\frac{J_{CL,2D}}{J_{CL,1D}} = 1 + \frac{0.3145}{W/D} - \frac{0.0004}{(W/D)^2} \tag{2.10}$$

where $J_{CL,1D}$ is the 1D CL formula drived in section 2.4.1. Later, an analytical formula for the same geometry is derived by Lau by using the assumption of $W/D >> 1$ [46]. The derived formula which is given in Equation 2.11 significantly fits with the empirical formula in Equation 2.10, which can be also seen in Figure 2.7. In the figure, a blue plot belongs to the formula in Equation 2.10 whereas a red plot corre-

sponds to the formula in Equation 2.11.

$$J_{CL,2D} = J_{CL,1D} \times \left(1 + \frac{D}{\pi W}\right) \tag{2.11}$$

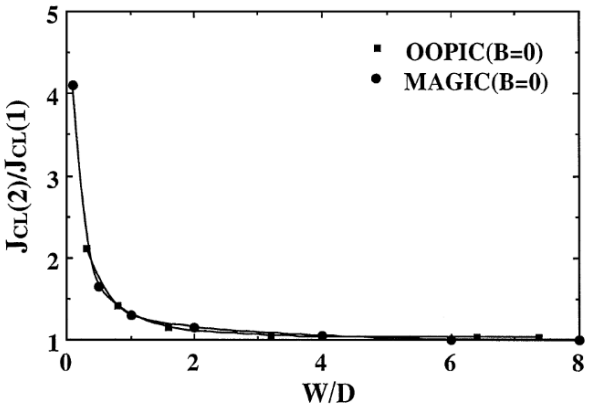

Figure 2.6: The normalized 2D CL current with respect to 1D CL law versus W/D graph in OOPIC and MAGIC [45].

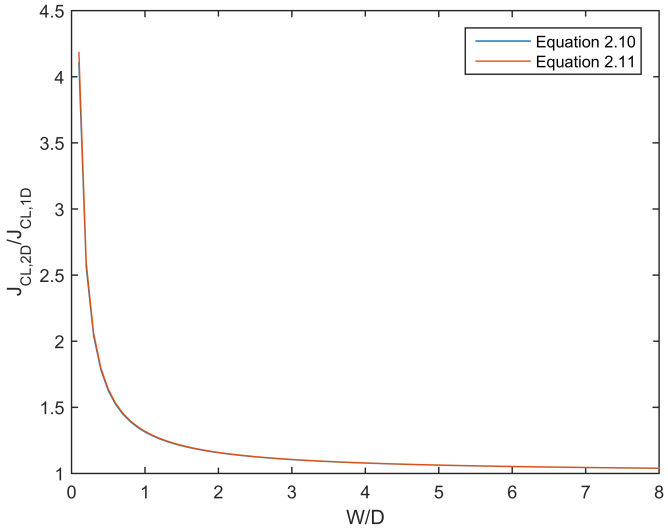

Figure 2.7: The plots of the normalized emitted current density formulas in Equation 2.10 and Equation 2.11.

In the same study, 2D CL formula for the circular emitter with radius R is also obtained by using the same procedure, which is stated in Equation 2.12. This formula is

confirmed by simulation base study, which is valid for $0.5 < R/D$ [47].

$$J_{CL,2D} = J_{CL,1D} \times \left(1 + \frac{D}{4R}\right) \tag{2.12}$$

Then, by using the similar analytical approach in [46], 3D CL formula is introduced for a planar and cylindrical diodes in classical and weakly relativistic regime by Koh and colleagues [48]. Furthermore, several emitter surface types, such as rectangle, ellipse, square,circle and triangle are studied in this work. The formula of 3D CL is written in the general form as follow:

$$J_{CL,3D} = J_{CL,1D} \times (1 + F \times G) \tag{2.13}$$

where F is the normalized mean position of 1D electron flow and G is the geometrical correction factor. F is used in order to evaluate the mean positions of the electrons. Thus, it is directly related with the applied voltage into diode. In the classical regime, the normalized emission energy $\epsilon = \frac{E_0}{eV_0}$ is defined. Then for $\epsilon << 1$, $F = 1/4$ while for $\epsilon >> 1$, F closes to $1/2$. In the relativistic regime, at zero emission energy, U is defined as $eV_0/m_e c^2$. Then, up to $U = 0.8$, $F = \frac{1}{4}(1 + \frac{3U}{28})$. For the highly relativistic regime, which is $U >> 1$ $F = 1/2$.

The geometrical correction factor, G is equal to $\frac{1}{R/D}$ for a circular emitter and $\frac{4}{\pi W/D}$ for a strip emitter. The accuracy of the derived formula is verified by using MAGIC simulation code. It is reported that the error is within 4% [48].

2.4.3 Non-Uniform Emission

Another approach to the emission from a finite cathode is wing structured electron emission. This approach is more realistic than the uniform emission assumption, which is valid for the formulation given in Section 2.4.2.It is known that electric field enhancement is observed from sharp emitting structure [49, 50]. Hence, the higher electron emission is expected at the edge of the emitter due to the lack of space charge right outside the edge of the emitter. Nonuniform electron emission is satisfied by supplying the unlimited electron emission and forcing the normal component of

the electric field at whole cathode surface[40]. The typical wing structure of 2D electron emission is shown in Figure 2.8. In the figure, a normalized emitting current density for 1D CL law is plotted as a function of a normalized cathode position for gap separation D, for different cathode width, W and gap separation, D pairs. (W, D) pair is given in Figure 2.8, as well.

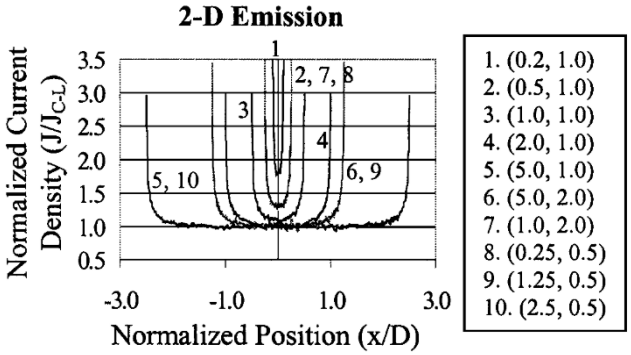

Figure 2.8: Typical wing structure of 2D electron emission [51].

In [52], the same 2D diode configuration in [45] is used by applying nonuniform approach. The variation on the normalized total current for W/D ratio is plotted, which can be seen in Figure 2.9.

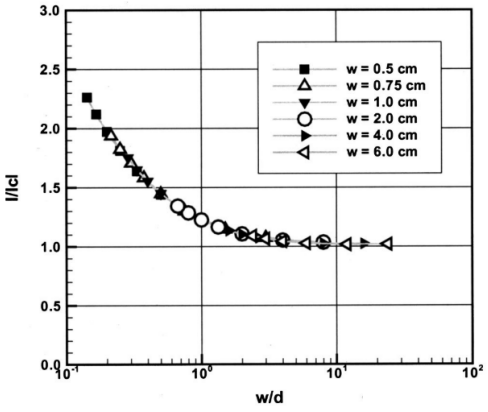

Figure 2.9: A normalized total current with respect to the 1D CL current versus ratio of W/D for different W values [52].

Then, this curve in Figure 2.9 is fitted with the formula below:

$$I_{CL,2D} = I_{CL,1D} \times \left(1 + \frac{0.23033}{W/D} - \frac{0.00665}{(W/D)^2}\right) \tag{2.14}$$

When the formulas given in Equation 2.10, Equation 2.11 and Equation 2.14 are plotted together, which is given in Figure 2.10, it is clear that the formula obtained from non-uniform emission approach qualitatively agrees with the formulas acquired from uniform emission approach.

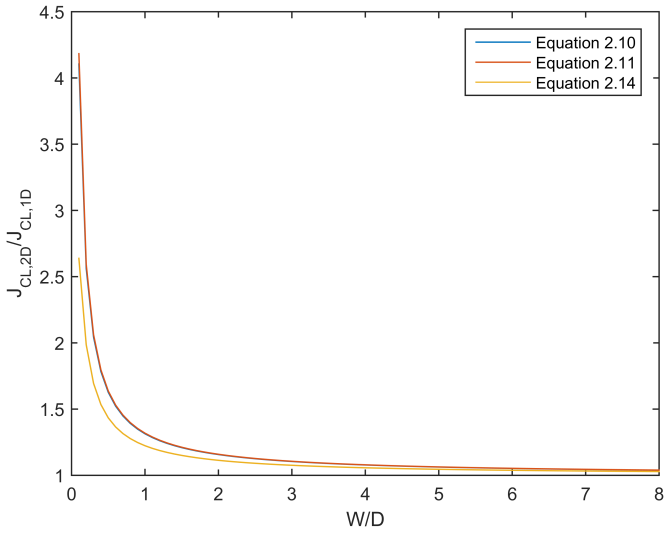

Figure 2.10: The plots of the normalized emitted current and current density formulas in Equation 2.10, Equation 2.11 and Equation 2.14.

Furthermore, in the nonuniform emission approach, it is observed that for the W/D ratio equal and greater than one, 1D CL law is followed in the center of the beam when a huge electron emission is observed at the edge of the beam. When the W/D ratio is smaller than one, the peak current value of the wing and the current at the center of the beam increase [47, 51, 52]. It is also shown that the wing structure is independent of the applied voltage V_0 [51].

Later, for the nonuniform approach, Rokhlenko and Lebowitz introduce a semi-analytical solution for a strip and a circular cathode shape [53]. The general form of the solution

is given in Equation 2.15.

$$I_{CL,2D} = I_{CL,1D} \times \left(1 + \alpha \frac{PD}{2S}\right) \tag{2.15}$$

where $\alpha = 0.19 + 0.48e^{-3.7\lambda}$, which λ is the width of non-emitting edge. Moreover, $\frac{PD}{2S}$ is equal to $\frac{D}{W}$ for the strip cathode and $\frac{D}{R}$ for the circular cathode.

When the formula in Equation 2.15 for different values of λ is plotted with the formulas in Equation 2.10 and Equation 2.14, it is obvious that the derived semi-analitical formula in Equation 2.15 give good aggrement with the simulation-based studies using different approaches.

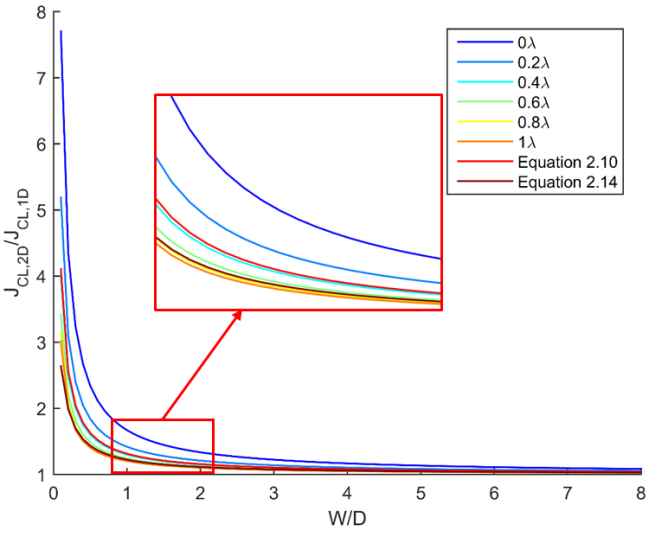

Figure 2.11: The plots of the normalized emitted current and current density formulas in Equation 2.15 for different values of λ, Equation 2.10 and Equation 2.14.

2.5 Space Charge Limiting Current in a Circular Drift Tube

The space charge limiting current in a drift tube, I_{SCL} is the critical parameter for the operation of the vircator. In this section, space charge limiting currents for an annular and solid beam in a circular drift tube are given. A cross-sectional view of the beams

can be seen in Figure 2.12. The radius of the drift tube is denoted as r_0. r_b is the mean radius for the annular beam while it corresponds to the radius of the solid beam. The injection of the beam through the drift tube is supplied by the cathode whose potential is $-V_0$. The formulas can be applied under the assumptions, which are listed below:

- The electrons in the beam are collisionless.
- The beam is axially homogeneous to eliminate the effect of time.
- The radial density and velocity of the beam are azimuthally symmetric.
- The beam is uniform in space and mono-energetic.

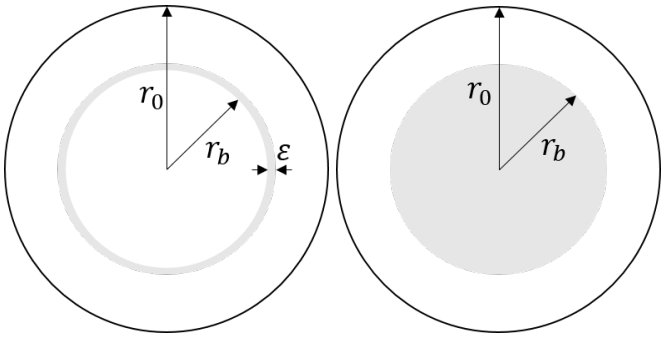

Figure 2.12: Cross-sectional view of (a)the annular beam and (b)the solid beam in a circular drift tube.

First, the annular beam is taken into consideration. For this purpose, one more assumption should be hold, which is to apply infinitely large external magnetic field in axial direction in order to satisfy an annular form for the beam.

For the annular beam, there is no space charge in the drift tube except at $r = r_b$. The Gauss' law in cylindrical coordinates given in Equation 2.16 can be rewritten for the regions $r < r_b$ and $r_b < r < r_0$ by equating the right hand side to zero. The beam potential on the axis is ϕ_b.

$$\nabla.\vec{D} = \rho_v \tag{2.16}$$

$$\frac{1}{r}\frac{d}{dr}\left(r\frac{d\phi}{dr}\right) = 0 \quad r < r_b \quad \& \quad r_b < r < r_0 \tag{2.17}$$

Thus, possible solutions for the beam potential for two different regions can be as follow:

$$\phi(r) = -\phi_b \quad r < r_b \tag{2.18}$$

$$\phi(r) = A + Bln(r) \quad r_b < r < r_0 \tag{2.19}$$

with the boundary conditions $\phi(r = r_b) = -\phi_b$ and $\phi(r = r_0) = 0$. Then, the beam potential can be obtain like in Equation 2.20.

$$\phi(r) = -\phi_b \frac{ln(\frac{r_0}{r})}{ln(\frac{r_0}{r_b})} \quad r_b < r < r_0 \tag{2.20}$$

The beam velocity, v_b and the beam potential on the axis, ϕ_b can be written in terms of the beam relativistic factor, γ_b as follow:

$$v_b = c(1 - (1/{\gamma_b}^2))^{1/2} \tag{2.21}$$

$$\phi_b = (\gamma_0 - \gamma_b)\frac{m_e c^2}{e} \tag{2.22}$$

where γ_0 is an injection energy of the electrons, which is equal to $1 + \frac{eV_0\ (kV)}{mc^2}$. Then, to satisfy continuity on the boundary $r = r_b$, Gauss' law in terms of potential $\phi(r)$ can be written, which is shown in Equation 2.23. Then, by integrating both side from ${r_b}^-$ to ${r_b}^+$, Equation 2.24 can be obtained.

$$\frac{1}{r}\frac{d}{dr}\left(r\frac{d\phi}{dr}\right) = \frac{en_b}{\epsilon_0} \quad at \quad r = r_b \tag{2.23}$$

$$r_b\left(\frac{d\phi(r = {r_b}^+)}{dr} - \frac{d\phi(r = {r_b}^-)}{dr}\right) = \frac{e}{\epsilon_0}\int_{{r_b}^-}^{{r_b}^+} n_b r dr = \frac{1}{2\pi v_b \epsilon_0}\int_{{r_b}^-}^{{r_b}^+} J_b 2\pi r dr \tag{2.24}$$

The second term on the left hand side is zero due to constant beam potential for inside the beam. Then, substituting Equation 2.20, Equation 2.21 and Equation 2.22

into Equation 2.24, the beam current, I_b can be written with respect to γ_b, which is given in Equation 2.25.

$$I_b(\gamma_b) = \frac{2\pi\epsilon_0 \frac{m_e c^3}{e}}{ln(r_0/r_b)}\left(1-\frac{1}{{\gamma_b}^2}\right)^{1/2}(\gamma_0-\gamma_b) = \frac{17\times10^3}{2ln(r_0/r_b)}\left(1-\frac{1}{{\gamma_b}^2}\right)^{1/2}(\gamma_0-\gamma_b) \quad (2.25)$$

If the obtained beam current formula in Equation 2.25 is plotted with respect to the beam relativistic factor, which is shown in Figure 2.13, it is clearly seen that I_b takes its maximum value for $\gamma_b = {\gamma_0}^{1/3}$. Then, the space charge limiting current for the annular beam which can be obtained as in Equation 2.26 [1, 19, 24, 27, 54, 55].

$$I_b(\gamma_b = {\gamma_0}^{1/3}) = I_{SCL,annular} = \frac{8.5\times10^3}{ln(r_0/r_b)}({\gamma_0}^{2/3}-1)^{3/2} \quad (2.26)$$

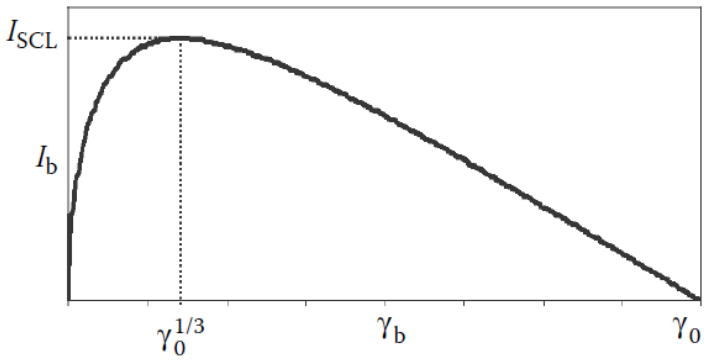

Figure 2.13: The beam current versus the beam relativistic factor plot [1].

If the same procedure is followed for the solid beam, its space charge limiting current can be obtained as follow [19, 27, 54, 56]:

$$I_b(\gamma_b = {\gamma_0}^{1/3}) = I_{SCL,solid} = \frac{17\times10^3}{1+2ln(r_0/r_b)}({\gamma_0}^{2/3}-1)^{3/2} \quad (2.27)$$

2.6 Microwave Generation and Frequency Spectrum

As mentioned in section 2.2, the source of the microwave generation is the back and forth motion of reflexing electrons and virtual cathode oscillation itself [18, 21, 26,

55, 57, 58, 59]. The frequency of virtual cathode oscillation, ω_{vc} can be equated to the beam plasma frequency, ω_p, which is given in Equation 2.28 [1].

$$\omega_{vc} = \omega_p = \left(\frac{n_b e^2}{\epsilon_0 m \gamma_0} \right)^{1/2} \tag{2.28}$$

Then, substituting Equation 2.5 into Equation 2.28, f_{vc} can be rewritten in more manageable form as follow:

$$f_{vc} = 1.3 \times 10^6 \sqrt{\frac{J_{CL}}{\beta\gamma}} \tag{2.29}$$

The formula in Equation 2.29 gives an approximated value for virtual cathhode frequency. The simulation studies show that the frequency of the virtual cathode oscillation varies as follow [23, 25, 56, 58]:

$$f_p \leq f_{vc} \leq \sqrt{2\pi} f_p \tag{2.30}$$

The value of $\sqrt{2\pi}$ is empirically found . In [23], it is also reported that if the injected current increases, the frequency of virtual cathode oscillation closes its maximum value.

The frequency of the trapped electrons between the real and the virtual cathode, which is named as reflexing frequency, f_r, is related with transit time between the real cathode and the anode. With the assumption that the distances between the virtual cathode and the anode and between the anode and the cathode are equal, the formula for the reflexing frequency can be written as follow [1, 56, 60, 61]:

$$f_r = \frac{1}{4T} = \frac{1}{4 \int_0^d \frac{dz'}{v_z}} \tag{2.31}$$

The formula given in 2.32 has a very well agreement with the simulation results as a main frequency [17, 20, 30, 62, 63]. Moreover, this formula can be drived for both

virtual cathode oscillation frequency in [64, 65] and the reflexing frequency [66].

$$f = \frac{c}{2\pi d} cosh^{-1}(\gamma_0) = \frac{c}{2\pi d} ln\Big(\gamma_0 + \sqrt{{\gamma_0}^2 - 1}\Big) \tag{2.32}$$

2.7 Mode Characteristics for a Circular Waveguide

In the case of the axial emission of the vircator in a circular waveguide, the space charge electrons are more likely to couple the radial electric field, E_ρ and the axial electric field E_z, which results in the microwave generation in TM_{0n} mode [1, 20, 21, 24, 56, 57, 58, 62, 67, 68, 69, 70]. Thus, the non-zero fields of TM_{0n}, which are E_ρ,E_z and H_ϕ can be seen in Equation 2.33, Equation 2.34 and Equation 2.35, respectively.

$$E_\rho = C\frac{k_z}{\omega\mu\epsilon}\left(\frac{x_{0n}}{r_0}\right) J_1\left(\frac{x_{0n}}{r_0}\rho\right) e^{-jk_z z} \tag{2.33}$$

$$E_z = -C\frac{j}{\omega\mu\epsilon}\left(\frac{x_{0n}}{r_0}\right)^2 J_0\left(\frac{x_{0n}}{r_0}\rho\right) e^{-jk_z z} \tag{2.34}$$

$$H_\phi = C\frac{1}{\mu}\left(\frac{x_{0n}}{r_0}\right) J_1\left(\frac{x_{0n}}{r_0}\rho\right) e^{-jk_z z} \tag{2.35}$$

where $k_z = \sqrt{k^2 - \left(\frac{x_{0n}}{r_0}\right)^2}$, r_0 is radius of a circular waveguide, x_{0n} is the n-th root of $J_0(x)$ and C is a constant.

Then, the cutoff frequencies of TM_{0n} modes can be found with the formula given in Equation 2.36 for the specified radius of the circular waveguide.

$$(f_c)_{0n}^{TM} = \frac{x_{0n}}{2\pi r_0\sqrt{\mu\epsilon}} \tag{2.36}$$

Radial distribution of non-zero E fields of the first two TM_{0n} modes, which are TM_{01} and TM_{02}, with respect to the normalized radial position are plotted in Figure 2.14. Moreover, the same radial distiribution with E_ρ in Figure 2.14a can be obtained for H_ϕ, as well. It is because H_ϕ field also contains $J_1(\rho)$ function, like E_ρ field.

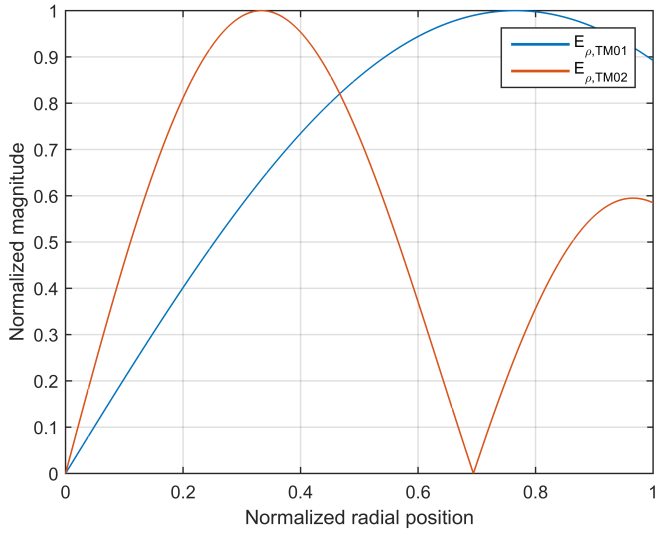

(a)

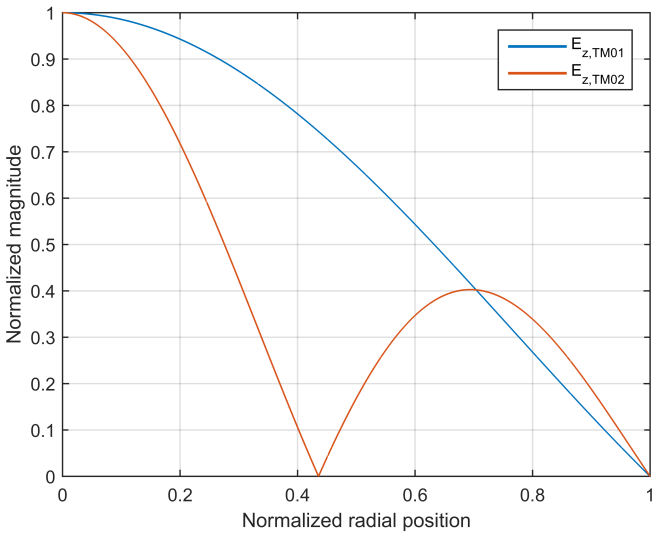

(b)

Figure 2.14: Theoretical radial distribution of (a)E_ρ (b)E_z of TM_{01} mode.

If the radius of the circular waveguide is chosen such that the microwave frequency of the vircator stays between the cutoff frequencies of TM_{01} and TM_{02} modes, it is guaranteed that the mode of the extracted microwave is TM_{01} mode [20, 60]. Hence, the limitation for the radius of the circular waveguide comes from this point. Non-zero E field densities of TM_{01} , which are E_ρ and E_z are given in Figure 2.15. As can be seen from Figure 2.15a, E_ρ field takes its maximum value at $r = 0.765 \times r_0$. On

the other hand, E_z field peaks at $r = 0$, which is shown in Figure 2.15b.

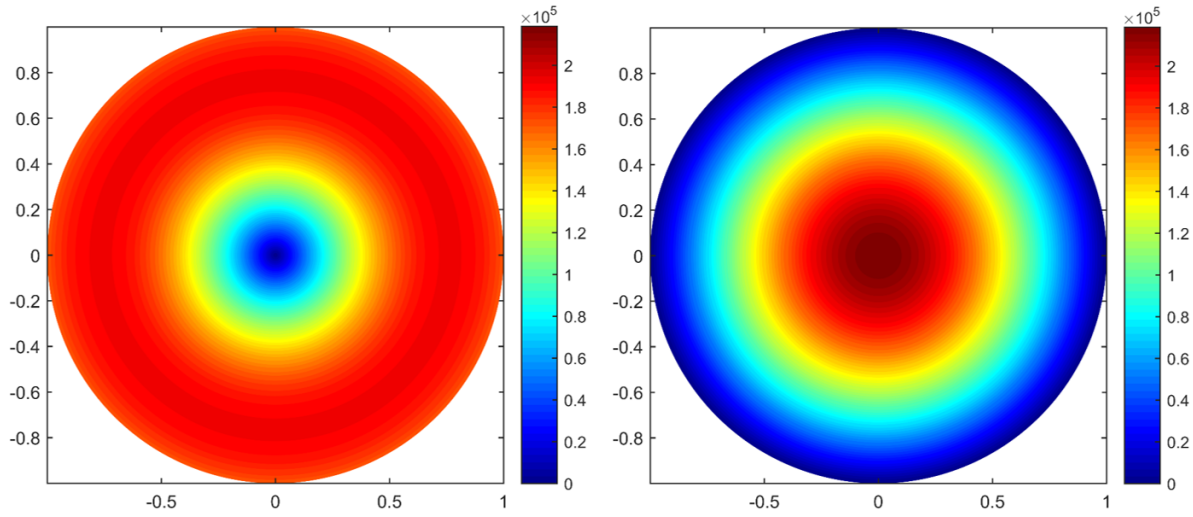

Figure 2.15: (a)E_ρ (b)E_z field density of TM_{01} mode.

In addition, a radiation pattern of the generated microwave is directly related with the transverse fields in an antenna aperture. If the mode of the produced microwave is conserved as TM_{01}, the only non-zero transverse E field in the aperture is obtained as E_ρ field, which is already given in Figure 2.15a. It is clearly seen in the figure that the radiation pattern of TM_{01} mode has null at the propagation axis. Hence, direct radiation cannot be properly achieved with TM_{01} mode. In order to overcome this radiation problem, the generated microwave in TM_{01} mode should be converted to another mode. In this manner, the transverse E field of the TE_{11} mode is given in Figure 2.16. It is obvious that the obtained power focuses on the radiation axis. Thus, it can be concluded that the produced microwave in TE_{11} mode can be radiated efficiently. At this point, TM_{01} to TE_{11} mode converter is an inevitable component for the axial vircator before the antenna stage.

In literature, several different configurations for a mode converter from TM_{01} to TE_{11} are available [71, 72, 73, 74, 75]. It is reported that a more than 90% efficiency can be achieved with the designed converters [72, 74].

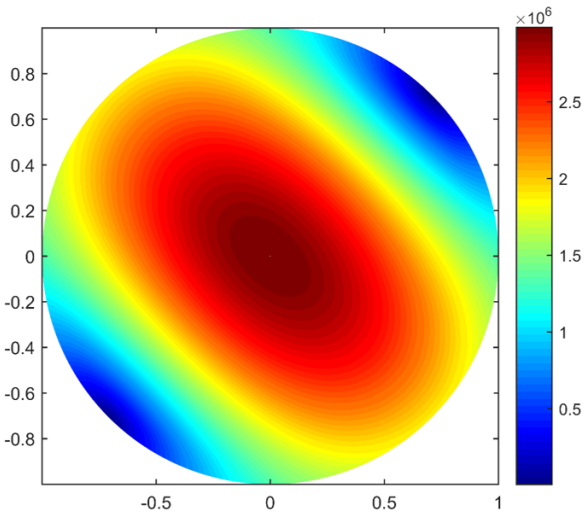

Figure 2.16: Transverse E field density of TE_{11} mode.

CHAPTER 3

SIMULATION SETUP

In this thesis, 3D Magic software is employed as a simulation program. It is one of the mostly used simulation programs in electromagnetic problems involving charged particles.

3.1 Overview of Magic

Magic is a FORTRAN based simulation software which employs electromagnetic particle-in-cell (PIC) and finite difference time domain (FDTD) methods together. It is aimed to simulate the interaction between charged particles and electromagnetic fields. For this purpose, first, both time and space are divided into finite pieces, which are named grids. After the selection of the desired spatial grids for three different dimensions, the time step for the simulation is determined by Magic itself without violating the Courant stability criterion. In order to satisfy this criterion, the formula, which is given in Equation 3.1 is used.

$$\chi^2 = c^2 \delta t^2 \sum_{i=1}^{N} \frac{1}{\delta x_i^2} \tag{3.1}$$

where χ is Courant ratio, δx_i is the cell size, N is the number of dimensions. The time step δt is calculated for $\chi = 0.85$ unless otherwise specified [76].

In Figure 3.1, time grid scheme in Magis is given. At each time step, first, Maxwell's equations are solved for all spatial grids. Later, by using the calculated E and B fields, the momentum, p, and the position, x of the charged particles are calculated by solving the Lorentz equation. After that, the continuity equation is solved to determine

both charge and current densities, ρ, and J, respectively. After that point, a new time step is proceeded by using charge and current densities of the previous time step as input. These calculations are repeated for each time step. Hence, fields and particles are advanced in time by computational loop.

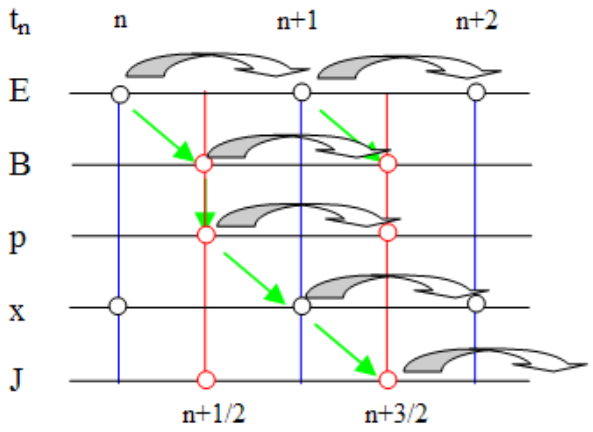

Figure 3.1: Time grid scheme in Magic [76].

It is crucial to note that the simulation variables given in Figure 3.1 are not calculated at the same time. These are associated with integer or integer+1/2 time steps, which is called a leap-frog algorithm.

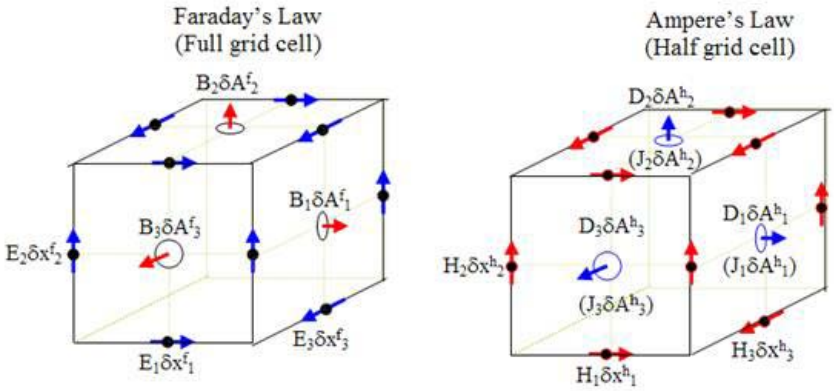

Figure 3.2: The sample of the full grid Yee cell and the half grid Yee cell which used in Magic algorithm [76].

Besides the leap-frog algorithm in time, Yee Cell formulation is utilized for the spatial grids in Magic. By introducing 3D Yee lattice, the same simulation variables are correlated with a full-cell or a half-cell positioning. The sample of the full grid Yee cell and the half grid Yee cell which used in Magic algorithm can be seen in Figure 3.2 [76, 77].

3.2 Simulation on Axial Vircator

3.2.1 Geometry of Axial Vircator

The polar coordinate system with (ρ, ϕ, z) coordinate notation is used in all simulations on the axial vircator. Based on the specified system, the axial vircator with its dimensions is drawn as in Figure 3.3. The longitudinal dimensions l_1, l_2 and d_{ak} indicate a length of the cathode, a length of the circular drift tube after the anode and an AK gap separation, respectively. On the other hand, the radial dimensions r_0, r_c and r_{cr} show a radius of a circular waveguide, the cathode and cathode ring, respectively. l_1, l_2 and r_0 are set to 120, 200 and 200 mm for all simulations whereas the other demonstrated dimensions are changed in some range to understand operation fundamentals of the axial vircator.

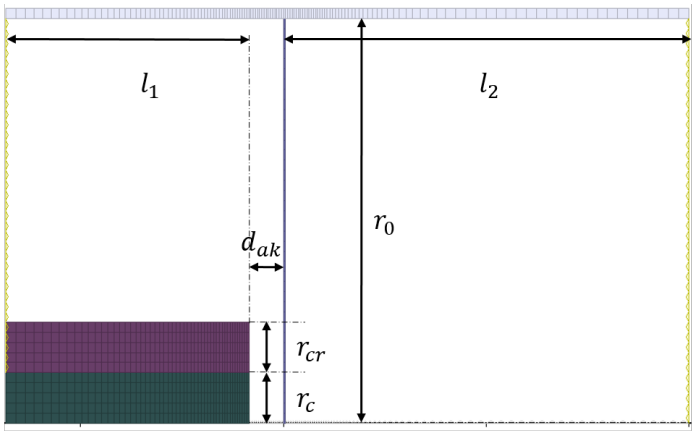

Figure 3.3: Cross-section in ρ-z plane of the axial vircator with dimensions.

3.2.2 Spatial Grid

The essential point in the spatial meshing of the axial vircator is the longitudinal grid resolution in the vicinity of the diode. It is advised to use 10 to 16 longitudinal mesh grids in that region by the support team of Magic. For this purpose, a variable is defined, which is named as NzGAP. The maximum value of the range, 16 is assigned as NzGAP to capture the depression of space charge between the cathode and the anode. In the other part of the geometry, longitudinal grids are released to shorten the time of simulation. Due to fixing NzGAP to the constant value, lessening in an AK gap separation causes a significant change in the simulation time.

Another factor which leads to a massive variation of simulation time is the number of the electrons released into the gap. Thus, enlargement of the emission surface results with an increase in the number of the electrons, which causes to increase in the simulation time, as well. Simulation time is roughly between three and twenty-one hours.

3.2.3 Excitation of Structure

The input of the vircator is in the shape of the coaxial line, which can be seen in Figure 3.4. A circular waveguide corresponds to the outer conductor of the coaxial line whereas the inner conductor of the coaxial line can be thought as the cathode with a cathode ring structure, if available. In the axial vircator, a potential difference between the cathode and the anode can be obtained by introducing an incoming wave to the input of the geometry. For this purpose, two different functions should be specified, which are a temporal function, $f(t)$ and the transverse directed spacial profile function, $\vec{g}_x(\vec{r})$. Then, the total field at the boundary can be shown as in Equation 3.2. In this thesis work, 3D Magis simulation software is used. Thus, two spatial profile functions should be defined, named as $\vec{g}_{x_1}(\vec{r})$ and $\vec{g}_{x_2}(\vec{r})$.

$$\vec{E}(\vec{r},t) = \vec{E}_i(\vec{r},t) + \vec{E}_o(\vec{r},t) = f(t)(\vec{g}_{x_1}(\vec{r}) + \vec{g}_{x_2}(\vec{r})) + \vec{E}_o(\vec{r},t) \qquad (3.2)$$

where E_i is the incoming wave and E_o is an outgoing wave. Moreover, for the axial vircator geometry in Figure 3.4, x_1 and x_2 are ρ and ϕ coordinates, respectively.

The temporal function for the axial vircator has 55 ns duration time, $t_{duration}$ with 20 ns rise time, t_{rise}. The typical temporal function form can be seen in Figure 3.5. This wave shape is obtained by using a smooth ramp function in Magic, which is given in Equation 3.3. The smooth ramp function, which is given in Equation 3.4, is also declared by Magic itself. The temporal function can be scaled by the desired flat region voltage value, V_{max}.

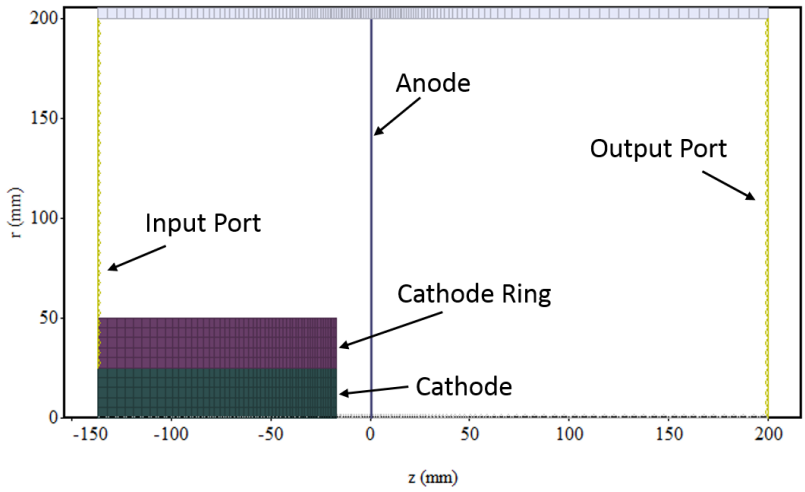

Figure 3.4: Cross-section in ρ-z plane of the axial vircator .

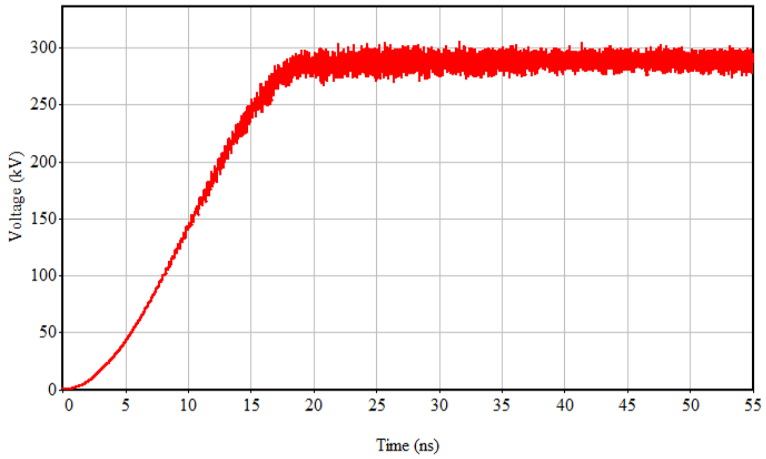

Figure 3.5: The applied temporal function wave shape to the input of the axial vircator by scaling with 288 kV.

$$f(t) = V_{max} SMOOTH\_RAMP(t/t_{rise}) \tag{3.3}$$

$$SMOOTH\_RAMP(t) = sin\left(\frac{\pi}{2} ramp(t)\right)^2 \tag{3.4}$$

where $ramp(t) = t$ for $t > 0$.

The spacial profile functions, $\vec{g}_\rho(\vec{r})$ and $\vec{g}_\phi(\vec{r})$ are chosen as in Equation 3.5 and Equation 3.6, respectively. With these functions, it is amied to satisfy the LAPLACIAN equation at the input port of the axial vircator.

$$\vec{g}_\rho(\vec{r}) = \frac{1}{r} \cdot \vec{a}_r \tag{3.5}$$

$$\vec{g}_\phi(\vec{r}) = 0 \cdot \vec{a}_\phi \tag{3.6}$$

It is crucial to note that if the formula in Equation 3.3 is directly applied to the geometry, the maximum value of the total voltage seen at the inlet of the axial vircator becomes different than the entered value into Magic due to reflecting wave, which can be seen in Equation 3.2. Hence, to obtain the same total voltage difference, V_{max} at the input port with the applied temporal function, rescale function is used by defining CIRCUIT command. In this way, the intended total voltage difference of the vircator can be achieved without requiring an iterative simulations process. The rescale function can be seen in Equation 3.7.

$$rescale(t) = \exp\left(\frac{1}{\delta t}\left(1 - \frac{\delta t}{t}\right)\int_0^t \left(1 - \frac{observed(t')}{desired(t')}\right)dt'\right) \tag{3.7}$$

where δt is the time step which is calculated by Magic by using the formula given in Equation 3.1.

3.2.4 Emission Process

Electron emission due to an explosive emission process naturally occurs by forming the plasma on the cathode surface, which is detailedly explained in section 2.3.

However, in Magic, instead of the plasma creation on the cathode surface, a phenomenological model is used to satisfy CL law in a diode region [76]. This kind of emission is provided by applying EMISSION EXPLOSIVE command. For this command, it is required to specify the threshold field, which is defined as the limit electric field for a breakdown. For any particular cell, if the threshold field is exceeded, the emission of electrons from that cell starts. Then, the non-emitting cell between two emitting cells is also forced to break down.

Then, with the EMIT command, the emission process is implemented for the specified part of the structure, which is the cathode in this case. It is crucial to note that the only allowed emission surface of the cathode is the surface which faces with the anode.

3.2.5 Anode Structure

An anode structure can be obtained by using FOIL command with two different models. The first model is a grid model, which can be seen in Figure 3.6. In this model, it is possible to give actual physical dimensions of an anode, which are widths and pitches for both transverse directions and a starting point for the anode. On the other hand, the second model is a fraction model. By defining a transmission fraction, a physical aperture of the anode is directly given to the simulation. In this thesis, the second model is utilized by specifying a fraction to 0.8 with a thickness of 1 μm.

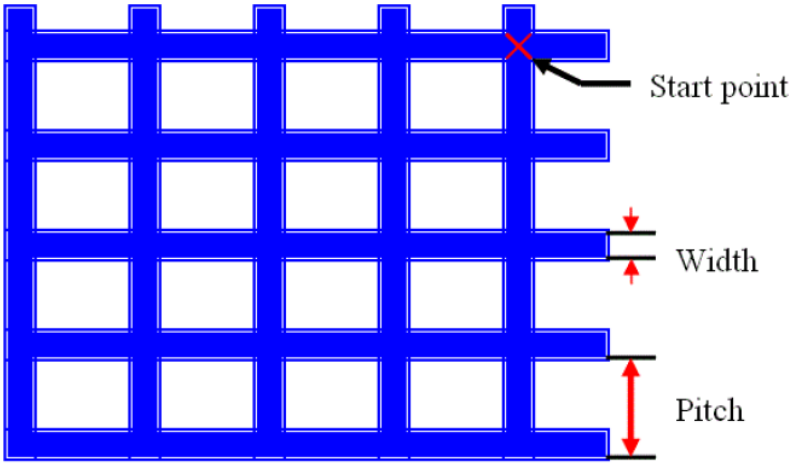

Figure 3.6: Typical anode structure for the grid model [76].

3.2.6 Diagnostics in Magic

In this thesis work, four main time plots are utilized. First, FIELD_INTEGRAL E.DL command is used to observe a voltage difference between specified two points. The voltage difference, V_{inlet} at the input port of the axial vircator and the AK gap voltage,V_{ak} are measured with this command.

In the same manner, FIELD_INTEGRAL H.DL command is used to measure current for defined loops. In addition to observing input current I_{inlet} of the axial vircator with this command, it is also possible to obtain radial current density profile for a specified longitudinal position with this command. In order to obtain a radial profile, current measurements are made by defining concentric loops for each radial grid point. Then, if subtracted the current value of the inner loop from the one of the current loop is divided into the annular area, current density profile can be calculated.

To measure power, OBSERVE FIELD_POWER command is utilized. Power is calculated by integrating the Poynting flux through a defined area. By using this command, the power at both the input and the output ports of the axial vircator are calculated on a defined input and output areas, respectively.

Another time plot is FIELD command. With this command, it possible to measure a strength of field on the desired area, which corresponds to the mean of the measured field over the area. In this thesis work, for field measurement, an area, which is defined at r-ρ plane with 1 cm distance from the output port of the geometry is used. A name of the area is denoted as field measurement area for simplicity in the next chapters. Field measurement can also be obtained for a single point. Thus, by utilizing field measurement at a point, mode analysis can be achieved. It is expected that the radial profile of fields' strengths for a specific frequency is fitted by the Bessel functions of the first kind, which correspond to radial distributions of TM_{0n} mode fields. The more information regarding field distribution of TM_{0n} mode can be found in section 2.7.

Besides time plots related to an electromagnetic wave, particle-based measurements can be made in Magic. By utilizing this PHASESPACE command, the momentum, the kinetic energy, the position and the charge of particles can be plotted. The most

well-recognized of these plots is longitudinal momentum versus distance plot. It gives a clue of whether the virtual cathode forms or not, which is detailedly discussed in the next chapter.

CHAPTER 4

SIMULATION ON THE AXIAL VIRCATOR

4.1 Effects of The Cathode Ring

According to several experimental studies in literature, the metallic bushing ring is utilized with the cathode [34, 35, 36, 41, 42, 78]. It is reported that a bushing ring offers an opportunity to durable experimental process [51]. With the cathode ring, it is also declared that more uniform emission is achieved by eliminating the edge effects of a finite cathode [51, 52, 79]. Furthermore, it is stated in a simulation-based study that the cathode ring structure is used to increase the power conversion efficiency of vircator [62]. Thus, the effects of the cathode ring structure are investigated in this section to attain more realistic cathode setup for experimental study by discussing its effects.

First, it is aimed to determine the optimum length of the cathode ring radius. For this purpose, it is swept from 0 to 100 mm for several specified values. In this study, the cathode ring radius is defined as the distance between its inner and outer radius, which is denoted as r_{cr} in section 3.2.1. The data taken from these simulations are tabulated in Table 4.1. The values for I_{emit} and P_{in} are obtained by taking the mean of a flat region of the measured wave shapes, which is between 20 and 55 ns. The values for the Max P_{out} are directly acquired as a maximum of the measured power for each simulation. Then, to obtain the values of the Mean P_{out}, first, the measured output power is filtered through a step filter. The step filtered output power for all simulations can be seen in Figure 4.1. Then, an output power window is defined. It starts at the point when the half of the maximum filtered output is obtained and lasts until the end of the simulation. Hence, the values of the Mean P_{out} is obtained by performing the average

of the filtered output power over the defined output power window. The last three columns of the Table 4.1 belong to three different efficiencies. In literature, several efficiency definitions exist. In this study, three different efficiencies are introduced as follows. First, the energy efficiency is obtained by dividing input energy into output energy of the axial vircator. For the maximum power efficiency, the numerator is the Max P_{out} whereas it is the Mean P_{out} for the mean power efficiency definition. The denominator of both max and mean power efficiencies are the same, which is P_{in}.

Table 4.1: The emitted current, the input power , the output power & efficiency values for different r_{cr} values with $V_{ak} = 288\ kV$, $d_{ak} = 17\ mm$ and $r_c = 35\ mm$.

r_{cr} (mm)	I_{emit} (kA)	P_{in} (GW)	Max P_{out} (MW)	Mean P_{out} (MW)	Energy Efficiency	Max Power Efficiency	Mean Power Efficiency
0	6.61	1.84	95.22	46.66	2.2	5.2	2.5
5	5.14	1.42	102.41	56.27	2.8	7.2	3.3
10	4.85	1.34	103.29	49.57	2.4	7.7	3.7
25	4.81	1.32	118.37	59.85	2.8	8.9	4.5
75	4.78	1.32	121.03	69.07	3.3	9.2	5.2
100	4.73	1.30	85.96	38.23	2.6	6.6	2.9

It is clearly observed from Table 4.1 that introducing a cathode ring to a certain extent enhances almost all efficiencies. It can be explained with that less fringing electric field in the vicinity of the emission surface supports space charge electrons to participate reflexing process rather than escape [62]. In order to see this effect of the cathode ring, the emitted electron flows for the simulations with and without defining the cathode ring are shown in Figure 4.2. A radius of the cathode ring in Figure 4.2b is 25 mm, and these snapshots are taken at t=4 ns. When these two snapshots are compared, to introduce a cathode ring provides minimizing the radial velocity of the electrons. Hence, it is concluded that the flow of electrons closes to 1D, which contributes more electrons to participating reflexing motion instead of leaking to a wall of the axial vircator. However, after a point, the efficiencies begin to drop. The reason is shown as the beam heating [62]. Beam heating causes electrons' scattering in axial momentum, and so all defined efficiencies decrease. This drop can be seen in

Table 4.1.

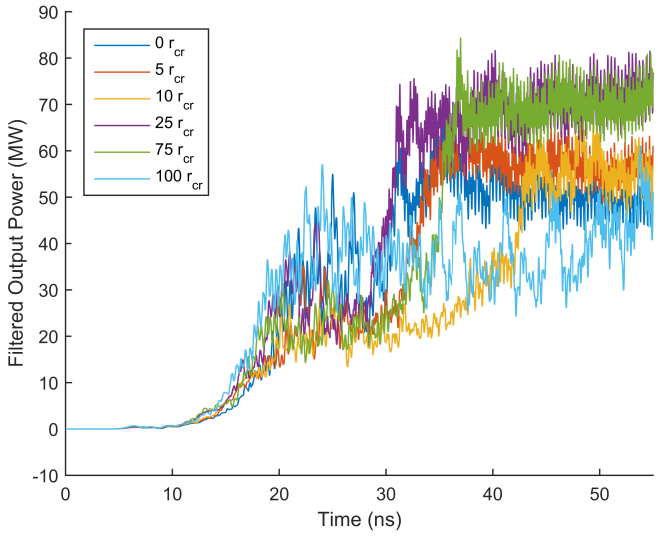

Figure 4.1: A step filtered output power versus time graphs for different r_{cr} values.

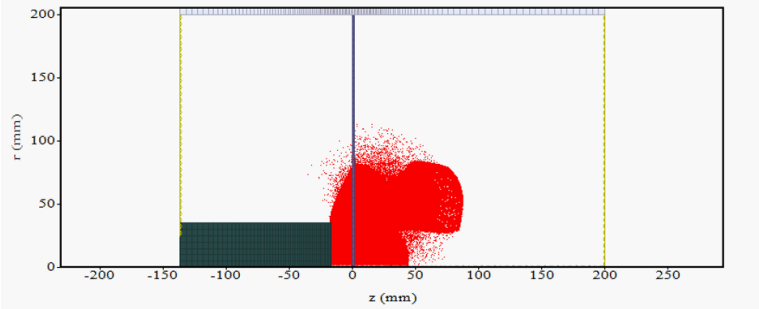

(a)

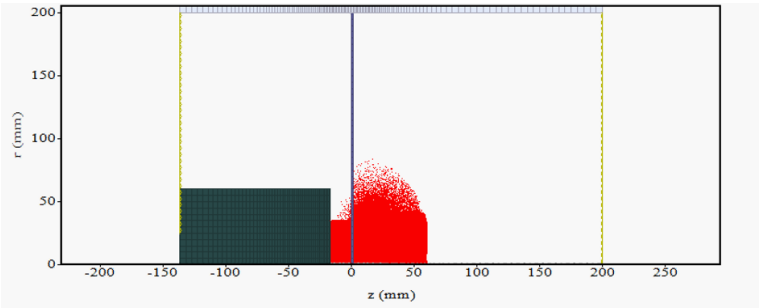

(b)

Figure 4.2: Snapshots at t=4 ns of the particle's position in rz plane (a)without (b)with 25 mm cathode ring.

Furthermore, a frequency spectrum of the generated electric field can be examined. In this sense, FFT of the E_z field for 25 mm and 100 mm radius of the cathode ring are given in Figure 4.3. In this figure, a red plot represents the simulation with the value of 25 mm r_{cr} whereas a blue plot shows the one with the value of 100 mm r_{cr}. At this point, it is important to note that the rest of the simulations have the same FFT characteristics with the one which has the value of 25 mm r_{cr} and, then to avoid confusion of plots, it is only plotted the FFT of the E_z field for the value of 25 mm r_{cr}. It is quite apparent in Figure 4.3 that when the cathode ring radius is determined as 100 mm, some extra frequency component arises, which causes the efficiency decrease. This is also explained with the long-familiar frequency splitting and mode competition phenomena [1, 20, 44, 60, 80, 81]. With these results, the optimum point for a radius of the cathode ring can be concluded as 75 mm.

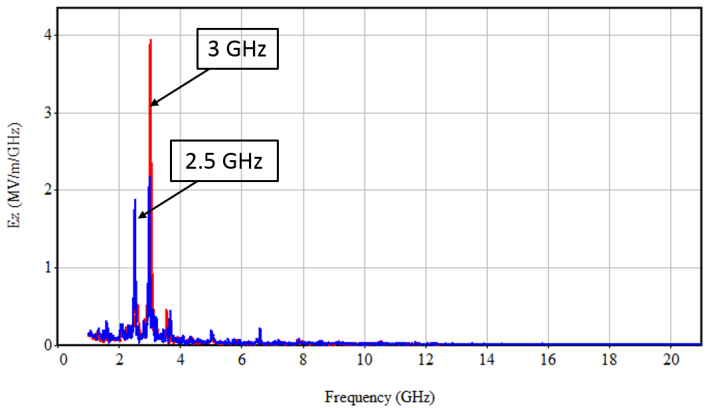

Figure 4.3: FFT of E_z field on the field measurement area for 25 mm and 100 mm cathode ring.

In addition to the effect of defining the cathode radius ring on the efficiency of the axial vircator, its effect on the electron emission can be studied. For this purpose, values of measured emitting current, I_{emit} for three different cathode radiuses, which are 10 mm, 25 mm and 35 mm are normalized by 1D CL current and, then for each cathode radius, the variations of the normalized emitting current by the cathode ring radius are plotted in Figure 4.4. It is obvious that to define the cathode ring causes a significant drop in the normalized emitting current for each cathode radius. After some values of r_{cr}, the normalized emitting current reaches its limit for all values of

cathode radius, which means that the edge effect of a finite cathode on the emitting current is almost negligible. The limit of the normalized emitting current for each cathode radius value is attained at the value of 25 mm r_{cr}.

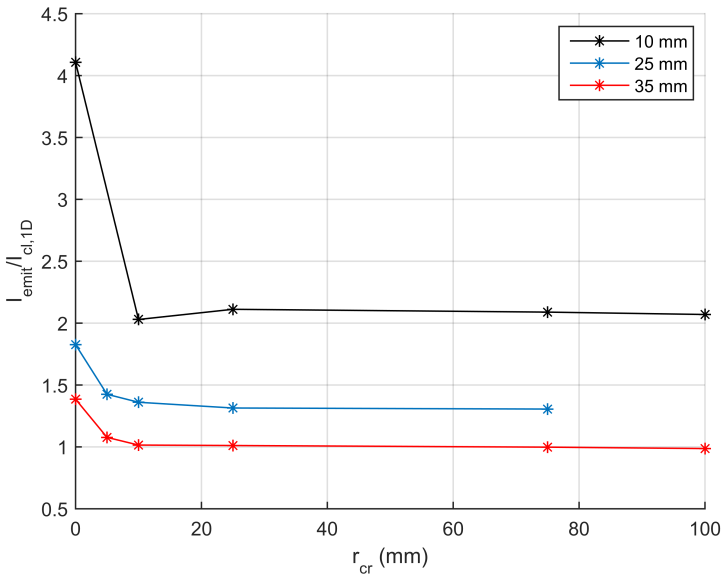

Figure 4.4: A variation of ratio with different r_{cr} values for 10 mm, 25 mm and 35 mm r_c.

As a result of this section, the cathode ring radius, r_{cr} can be fixed to the value of 25 mm when the physical size of the cathode ring is considered, as well. After this part of the thesis, the radius of the cathode ring is selected as 25 mm.

4.2 The Effect of The Space Charge Limiting Current on The Emitting Current

In many studies, it is reported that the emitting current follows the CL law [37, 42]. In this section, it is aimed to analyze the emitting current behavior of the axial vircator. For this purpose, d_{ak} which is one of the most important parameters of the vircator is changed from 5 mm to 40 mm with 5 mm steps and additional simulations are run for 7 mm and 17 mm d_{ak} values. The obtained current values for the simulations are listed in Table 4.2. The listed values of the emitted current,I_{emit} are obtained in the same way described in the previous section. The 1D and 2D CL currents, $I_{CL,1D}$

and $I_{CL,2D}$ are calculated with the formulas in Equation 2.9 and 2.12 by taking V_{ak} as 288 kV and the emission area is simply $\pi {r_c}^2$. I_{af} is measured just after the foil whereas I_{avc} is obtained at the field measurement area, which is defined after the point of virtual cathode formation. The last column of Table 4.2 gives the normalized emitting current.

Table 4.2: AK gap separation, the emitted current, the 1D CL current, the 2D CL current, the measured current after the foil, the measured SCL current & the normalized emitting current values for $V_{ak} = 288\ kV$ and $r_c = 25\ mm$.

d_{ak} (mm)	I_{emit} (kA)	$I_{CL,1D}$ (kA)	$I_{CL,2D}$ (kA)	I_{af} (kA)	I_{avc} (kA)	$I_{emit}/I_{CL,1D}$
5	18.37	27.96	29.36	5.64	0.40	0.66
7	11.64	14.37	15.37	4.46	0.45	0.81
10	7.48	7.03	7.73	3.14	0.36	1.06
15	3.93	3.13	3.60	2.08	0.26	1.26
17	3.12	2.44	2.86	1.80	0.29	1.28
20	2.42	1.76	2.12	1.47	0.43	1.37
25	1.60	1.13	1.41	1.03	0.95	1.42
30	1.14	0.79	1.02	0.76	0.71	1.46
35	0.87	0.58	0.78	0.59	0.56	1.51
40	0.70	0.44	0.62	0.49	0.46	1.59

As expected, an increase in AK gap separation causes a decrease in I_{emit} from the formula in Equation 2.9. The following three current values also have a decreasing trend as they are directly affected by I_{emit}. However, I_{avc} almost have similar values until the value of 25 mm d_{ak}.It is because I_{avc} is related to the space charge limiting current, I_{SCL}, which is described in Section 2.5 rather than the emitting current, I_{emit}. I_{avc} represents the current due to non-reflecting electrons. Thus, it is expected that I_{avc} is equal to the space charge limiting current of the specified geometry. On the other hand, by using Equation 2.26 and Equation 2.27, the space charge limiting current for the annular and the solid beams can be obtained as 0.83 and 0.67, respectively. The same difference between the values of the measured I_{avc} and the calculated I_{SCL} is reported in [56], too. The reason behind the disparity is that both I_{SCL} values are

calculated by ignoring the effects of the disturbance of an anode existence and the absorption of the emitted electrons by the wall of the geometry.

If the values of I_{avc} for simulations which have a larger d_{ak} value than 20 mm are examined, a decreasing trend with the almost same values of I_{af} can be observed. The reason is that for the geometry, which has a larger d_{ak} value than 20 mm, the virtual cathode cannot be formed. The all injected current to the drift tube, I_{af} can pass through without exposing to any reflexing. The proof of this claim can be seen in Figure 4.5, which are snapshots of a longitudinal electron phase-space diagram. It is the known that the observation of diamond shape implies the formation of the virtual cathode [1, 20, 29, 82]. For the simulations, which have a larger d_{ak} value than 20 mm, the diamond shape cannot be observed, which means there are not any reflected electrons back. Furthermore, it can be concluded that geometry for a larger d_{ak} value than r_c cannot form the virtual cathode.

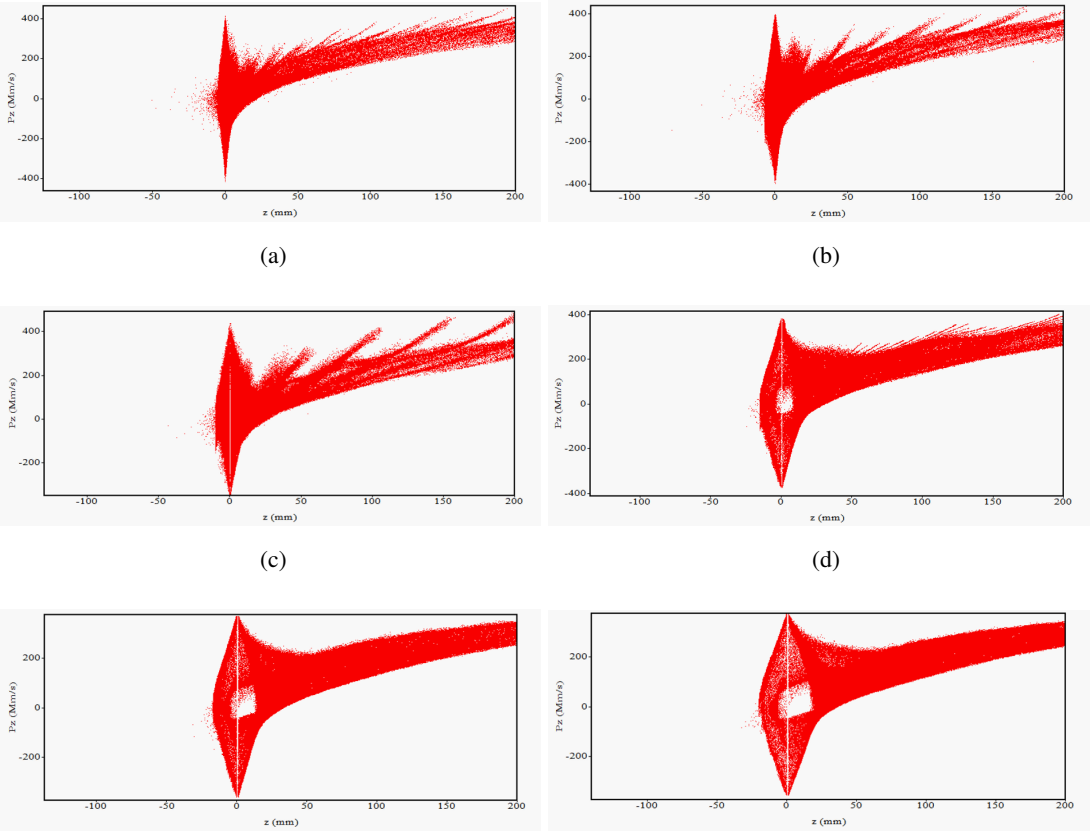

(a) (b)

(c) (d)

(e) (f)

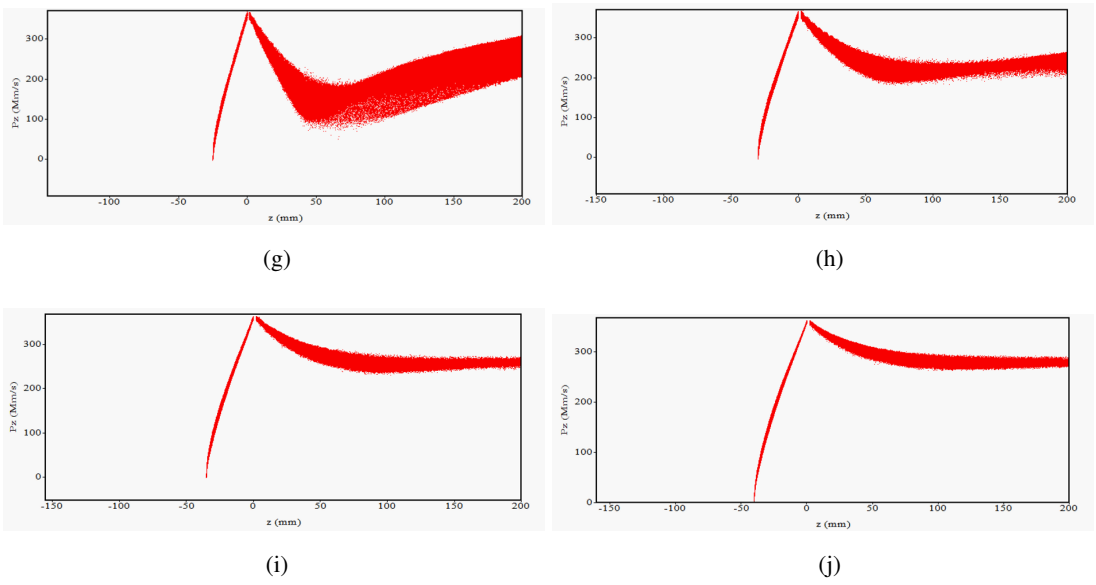

Figure 4.5: Snapshots of a longitudinal electron phase-space (P_z-z) diagram for (a)5 mm (b)7 mm (c)10 mm (d)15 mm (e)17 mm (f)20 mm (g)25 mm (h)30 mm (i)35 mm (j)40 mm AK gap separation with $V_{ak} = 288\ kV$ and $r_c = 25\ mm$.

A variation on the normalized emitting current given in Table 4.1 versus r_c/d_{ak} ratio is plotted, which can be seen in Figure 4.6. This plot has almost the same trend as the one in literature. However, for a large value of r_c/d_{ak} ratio, the normalized emitting current does not converge to unity. In [83], it is stated a similar result for the variation of the normalized current, as well. The underlying reason for the normalized emitting current's not approaching unity is explained as a sharp turn-on of the emission in this study. A short rise time of the injected current density to a diode causes an inductive behavior, and then the inductive voltage. The resultant voltage causes to slow down electrons' more quickly. It is also reported that the variation approaches unity for a large value of r_c/d_{ak} ratio when the injection with the relatively longer rise time. In this study, a 2D planar diode structure is examined with uniform emission assumption and then 2D CL current is defined as the limit of steady-state behavior of the diode, which corresponds to the formation of a virtual cathode in the diode. The study differs from this thesis work at this point. It is because the formation of the virtual cathode in the axial vircator is observed in a drift tube region rather than a diode region and a value of limiting current for the axial vircator is determined by the diode region, as

well.

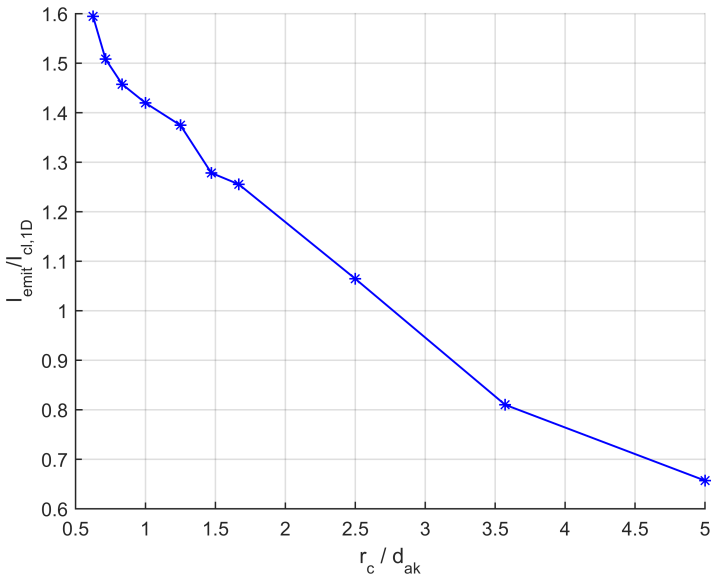

Figure 4.6: The normalized emitting current with respect to the 1D CL current versus r_c/d_{ak} ratio graph with the change of d_{ak}.

To suggest a fulfilling explanation to the situation in Figure 4.6, the normalized current density profiles for each d_{ak} value are obtained at three different locations in the diode region, which are the cathode surface, the middle of the gap and the anode surface. These profiles can be seen in Figure 4.7. In these profiles, it is observed the wing-like structure for 5 mm, 7 mm and 10 mm d_{ak} values. The reason of the wing-like structure can be stated as an excess of reflexed electrons' existence. It is because for smaller values of d_{ak}, the emitting current, I_{emit} increases with the rate of nearly ${d_{ak}}^2$ while the space charge limiting current for the structure nearly stays the same. Thus, it is concluded with the most of the electrons turn back into the diode region for smaller d_{ak} values, which causes a disturbance of the electron beam flow in the diode. In literature [20], a similar distortion of the electron flow is stated for the case of the formation of the virtual cathode. However, when snapshots in Figure 4.5 are examined, a wing-like structure cannot be observed in the simulations which has 15 mm, 17 mm and 20 mm d_{ak} although the virtual cathode formation occurs. Hence, it is clear that disturbance of the electron beam flow in the diode region is related with an excess of reflexed electrons' existence.

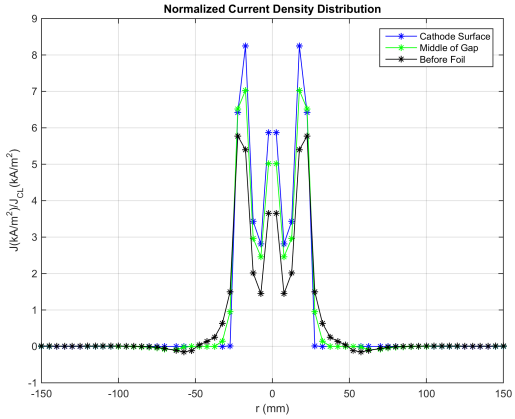
Normalized Current Density Distribution
Cathode Surface
Middle of Gap
Before Foil
J(kA/m²)/J_CL (kA/m²)
r (mm)

(a)

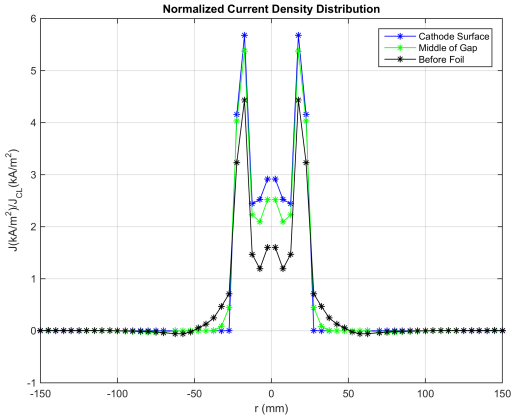
Normalized Current Density Distribution
Cathode Surface
Middle of Gap
Before Foil
J(kA/m²)/J_CL (kA/m²)
r (mm)

(b)

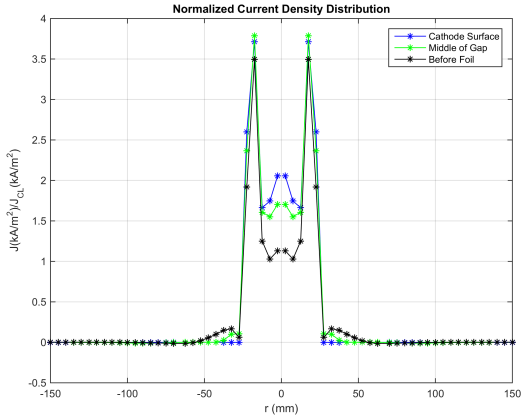
Normalized Current Density Distribution
Cathode Surface
Middle of Gap
Before Foil
J(kA/m²)/J_CL (kA/m²)
r (mm)

(c)

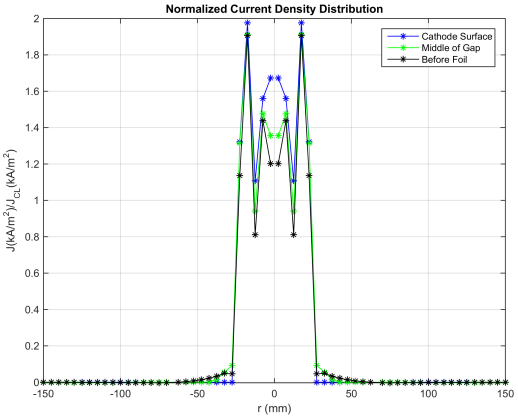
Normalized Current Density Distribution
Cathode Surface
Middle of Gap
Before Foil
J(kA/m²)/J_CL (kA/m²)
r (mm)

(d)

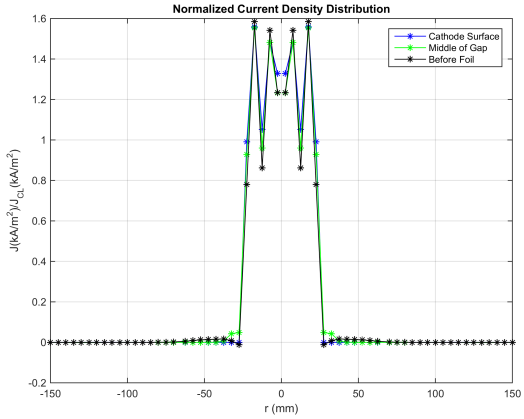
Normalized Current Density Distribution
Cathode Surface
Middle of Gap
Before Foil
J(kA/m²)/J_CL (kA/m²)
r (mm)

(e)

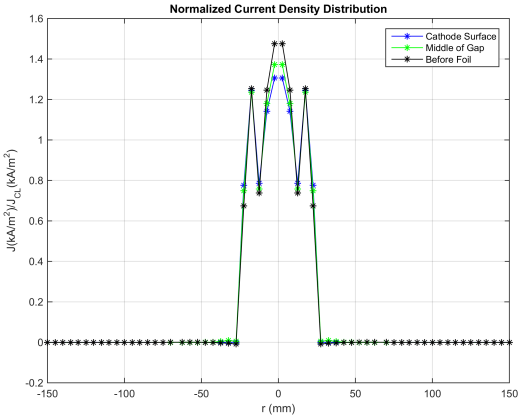
Normalized Current Density Distribution
Cathode Surface
Middle of Gap
Before Foil
J(kA/m²)/J_CL (kA/m²)
r (mm)

(f)

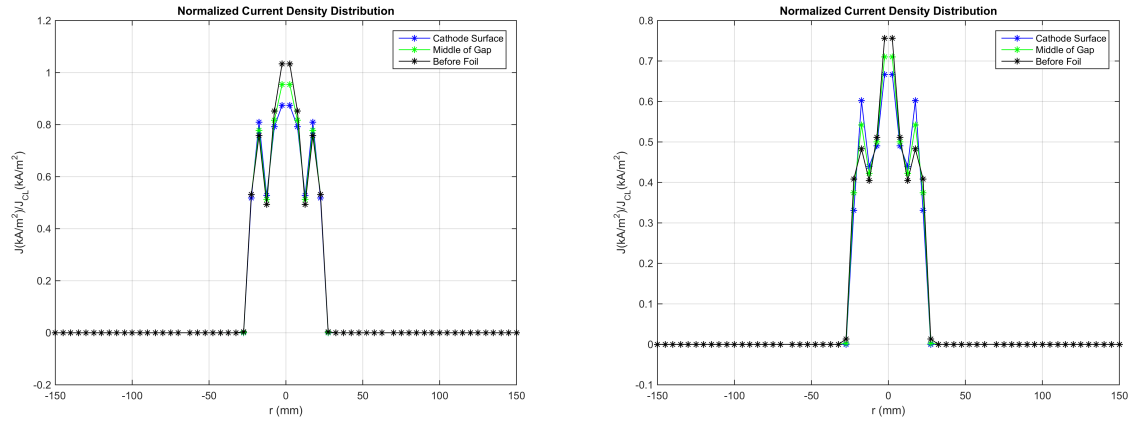

(g)

(h)

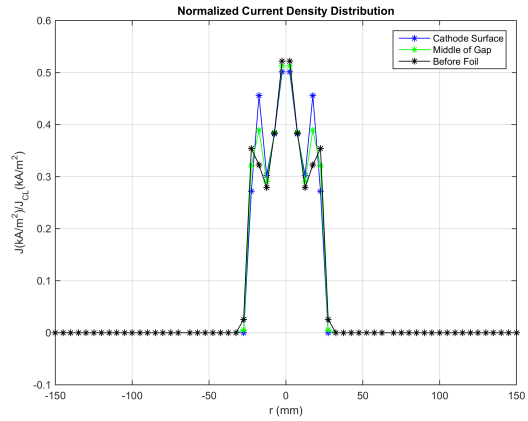

(i)

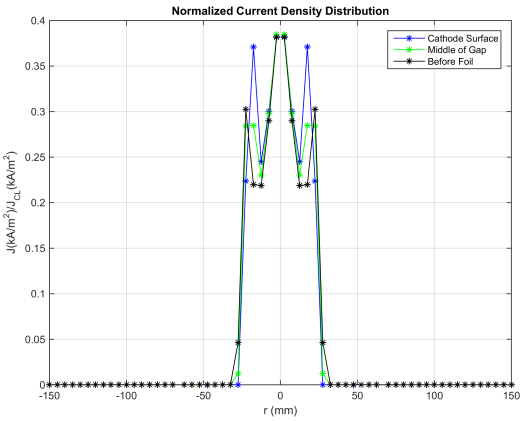

(j)

Figure 4.7: Normalized current density profile at the cathode surface, the middle of the gap and the anode surface for (a)5 mm (b)7 mm (c)10 mm (d)15 mm (e)17 mm (f)20 mm (g)25 mm (h)30 mm (i)35 mm (j)40 mm AK gap separation with $V_{ak} = 288\ kV$ and $r_c = 25\ mm$.

According to the observations given above, it can be deduced that the normalized emitting current plotted in Figure 4.6 is less than or almost equal to unity in the case of the excess of reflexed electrons' existence, which can be observed if $I_{SCL} << I_{emit}$.

The d_{ak} sweep is also performed for both $V_{ak} = 200\ kV$ and $V_{ak} = 400\ kV$. Then, the variation of the normalized emitting current for all voltage values is given in Figure 4.8. It can be clearly observed the same variation of the normalized emitting

current for all voltage values. Hence, the effect of the change in the applied voltage can be negligible. It is because the 1D CL current is directly proportional with ${V_{ak}}^{3/2}$ whereas the space charge limiting current for the circular drift tube is almost proportional with ${V_{ak}}^{3/2}$. Thus, the proportion of these two critical currents of the axial vircator stays nearly the same and any remarkable change in results cannot be observed.

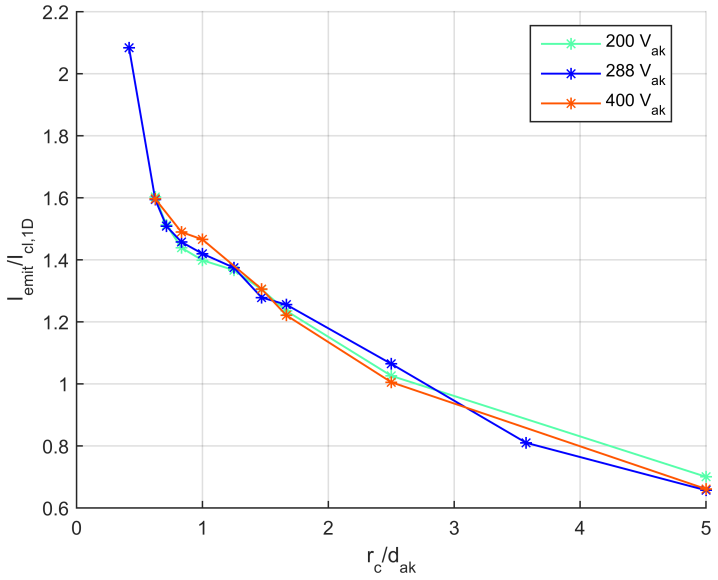

Figure 4.8: The normalized emitting current with respect to the 1D CL current versus r_c/d_{ak} ratio for $V_{ak} = 200\ kV$, $V_{ak} = 288\ kV$ and $V_{ak} = 400\ kV$.

Here, the cathode radius, r_c is swept, as well. The cathode radius is changed from 25 mm to 45 mm with 5 mm steps, and additional simulation is performed for 85 mm r_c value. The obtained data for these simulations are tabulated in Table 4.3. It is also important to note that the virtual cathode can be formed for all simulations. An increase on a radius of the cathode leads to rise of first four currents of Table 4.3, which are I_{emit}., $I_{CL,1D}$, $I_{CL,2D}$ and I_{af}. In contrast to the behavior of I_{avc} on d_{ak} sweep, I_{avc} slightly increases due to its proportion with $\frac{1}{ln(r_c)}$ for r_c sweep. Despite the increase in I_{avc}, the wing-like structure in a diode can also be observed for a larger value than 30 mm r_c due to an increment of I_{emit} with the square of r_c. These wing profiles can be seen in Figure 4.10. The variation of the same variation of the normalized emitting current is also plotted in Figure 4.9 with respect to r_c/d_{ak} ratio.

The normalized emitting current is obtained almost equal to or lower than the unity for simulations which has a wing-like current density profile in a diode.

Table 4.3: The cathode radius, the emitted current, the 1D CL current, the 2D CL current & the normalized emitting current values for $V_{ak} = 288\ kV$ and $d_{ak} = 17\ mm$.

r_c (mm)	I_{emit} (kA)	$I_{CL,1D}$ (kA)	$I_{CL,2D}$ (kA)	I_{af} (kA)	I_{avc} (kA)	$I_{emit}/I_{CL,1D}$
25	3.04	2.44	2.86	1.80	0.29	1.28
30	3.78	3.51	4.01	2.23	0.31	1.11
35	4.65	4.78	5.36	2.59	0.41	1.01
40	5.40	6.26	6.92	2.89	0.42	0.91
45	6.23	7.92	8.67	3.30	0.56	0.83
85	13.50	28.25	29.66	7.18	0.87	0.57

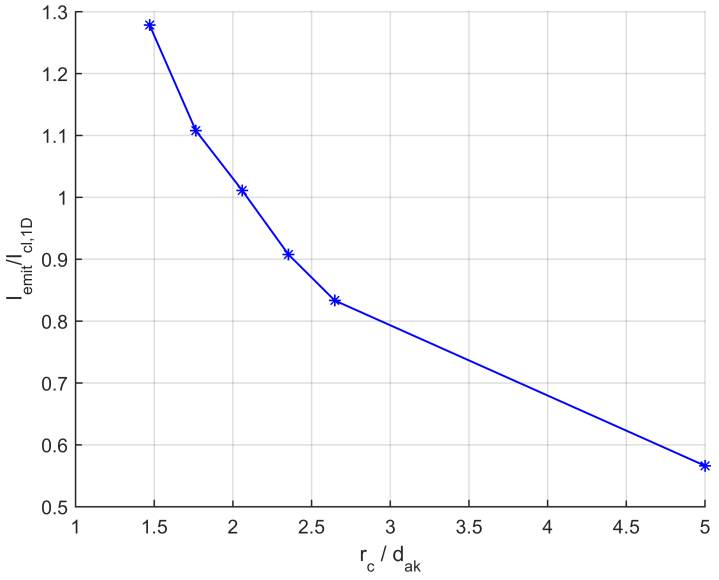

Figure 4.9: The normalized emitting current with respect to the 1D CL current versus r_c/d_{ak} graph with the change of r_c.

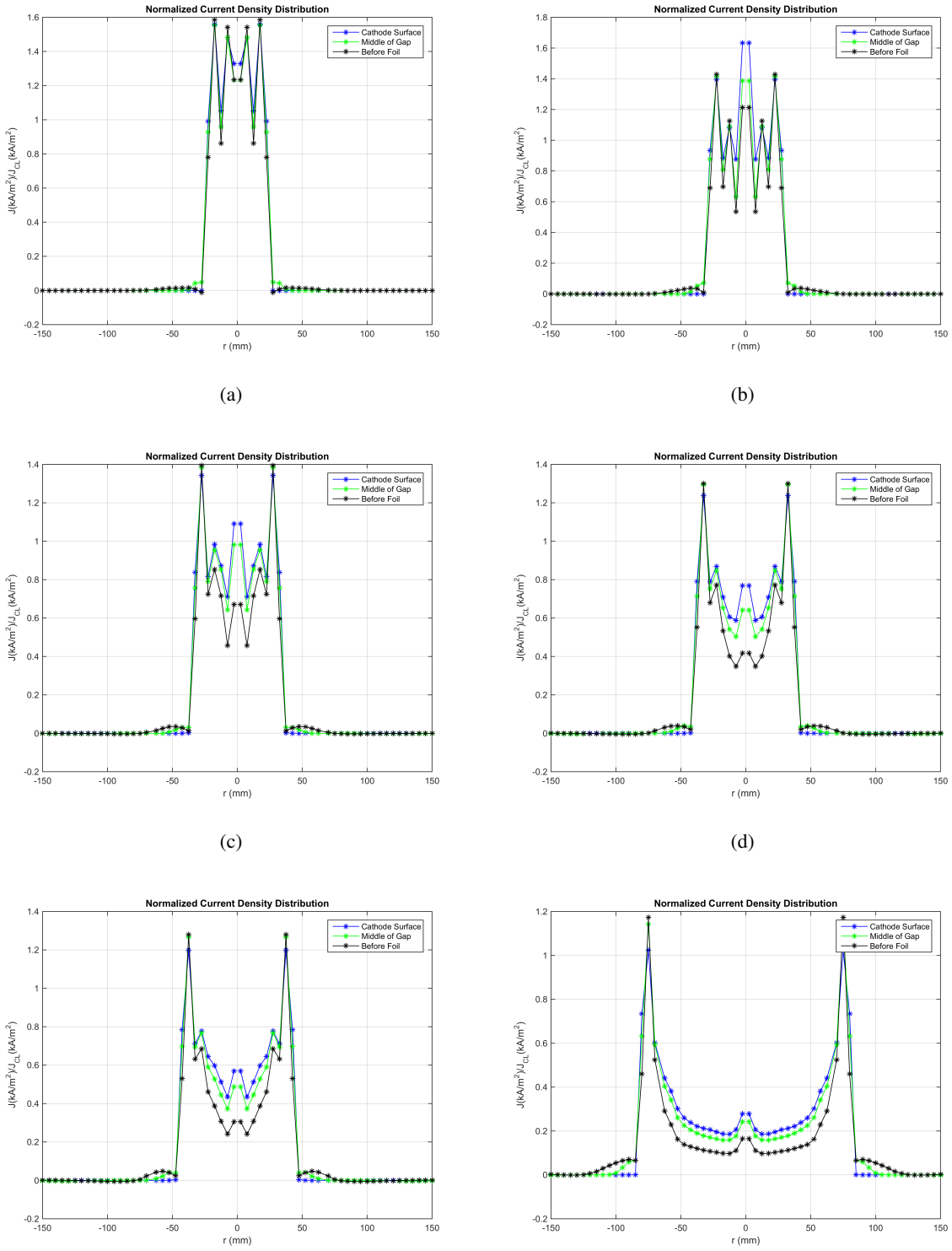

Figure 4.10: Normalized current density profile at the cathode surface, the middle of the gap and the anode surface for (a)25 mm (b)30 mm (c)35 mm (d)40 mm (e)45 mm (f)85 mm the cathode radius with $V_{ak} = 288\ kV$ and $d_{ak} = 17\ mm$.

4.3 The Effect of The Space Charge Limiting Current on The Efficiency of the Axial Vircator

The observation of the effect of the space charge limiting current on the emitting current is explained so far. In addition to that, the effect of the space charge limiting current on the efficiency of the axial vircator will be observed in this section. Table 4.4 belongs to d_{ak} sweep in which the virtual cathode can form. In the meantime, data of r_c sweep are tabulated in Table 4.5. In both tables, three different efficiency values are listed. According to these tables, the optimum efficiency values for the axial vircator are obtained in the case of the excess of the reflected electrons' existence, which implies that the ratio between I_{emit} and I_{SCL} affects not only the emitting current but also the efficiency of the axial vircator. In the light of these results, it can be concluded that if the excess of reflexed electrons' existence is promoted, this mechanism dominates the generation of microwave and increases the efficiency of the axial vircator.

Table 4.4: The AK gap separation, the normalized emitting current and three defined efficiencies for $V_{ak} = 288\ kV$ and $r_c = 25\ mm$.

d_{ak} (mm)	$I_{emit}/I_{CL,1D}$	Energy Efficiency	Max Power Efficiency	Mean Power Efficiency
5	0.66	1.9	3.0	2.0
7	0.81	3.3	6.9	3.5
10	1.06	3.5	7.9	3.9
15	1.26	1.4	2.3	1.6
17	1.28	1.3	1.8	1.6
20	1.37	2.0	2.6	2.1

The only exception regarding the efficiency pertains to the simulation which has 5 mm d_{ak}. Apart from the simulations with 7 mm and 10 mm d_{ak}, relatively lower efficiency is observed for the case of 5 mm d_{ak}. In order to comprehend the reason for low efficiency, it is appropriate to investigate the frequency spectrum of the generated microwave field. For this purpose, FFT of the E_z field for 5 mm d_{ak} is plotted in

Figure 4.11 with the E_z field, itself. By using the formula in Equation 2.32, the main frequency of the vircator is calculated as 9.68 GHz for 5 mm d_{ak}. It is obvious that the splitting a main frequency of the axial vircator around its theoretical value causes a decrease in the efficiency.

Table 4.5: The cathode radius, the normalized emitting current and three defined efficiencies for $V_{ak} = 288\ kV$ and $d_{ak} = 17\ mm$.

r_c (mm)	$I_{emit}/I_{CL,1D}$	Energy Efficiency	Max Power Efficiency	Mean Power Efficiency
25	1.28	1.3	1.8	1.6
30	1.11	1.4	2.2	1.6
35	1.01	3.8	8.9	4.5
40	0.91	2.9	6.1	3.1
45	0.83	3.7	7.7	3.9
85	0.57	4.5	9.8	4.8

As explained in Section 2.7, the axial vircator is prone to microwave generation in TM_{0n} modes. The four distinct frequency components of the axial vircator for 5 mm d_{ak} given in Figure 4.11b are examined in this respect.In order to determine a mode of each frequency component of the E_z field, field measurement at a point for the desired frequency used and, then radial field distribution is compared with the Bessel function of the first kind. A radial profile of E_ρ and E_z fields with corresponding the Bessel function can be seen in Figure 4.12. Due to an inadequacy of the radial spatial griding, perfect match cannot be obtained but it is sufficient to identify modes of the generated microwave for each frequency. For the frequencies 8.5 GHz, 9.2 GHz, 9.8 GHz and 10.7 GHz, modes of microwave are determined as $TM_{0,12}$, $TM_{0,13}$, $TM_{0,14}$ and $TM_{0,15}$, respectively. However, $TM_{0,15}$ mode cannot exactly follow its theoretical distribution. The underlying reason can be an occupation of more than one mode for that frequency component. In such cases, it is not easy to determine the exact modes of fields as Magic provides the only total field at the desired frequency. A x_{np} value, a cutoff frequency, and the main frequency of the aforementioned modes of TM_{0n} are tabulated in Table 4.6, as well. Values of f_{cutoff} and f_{op} are close each

other. However, f_{cutoff} is larger than f_{op}, which can be due to a numerical error of the simulation program.

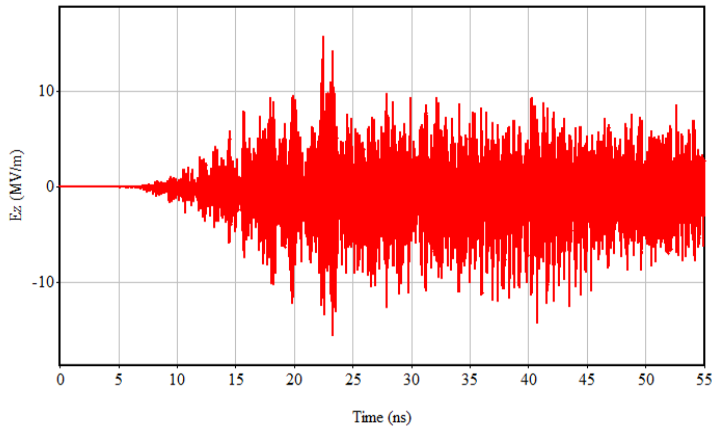

(a)

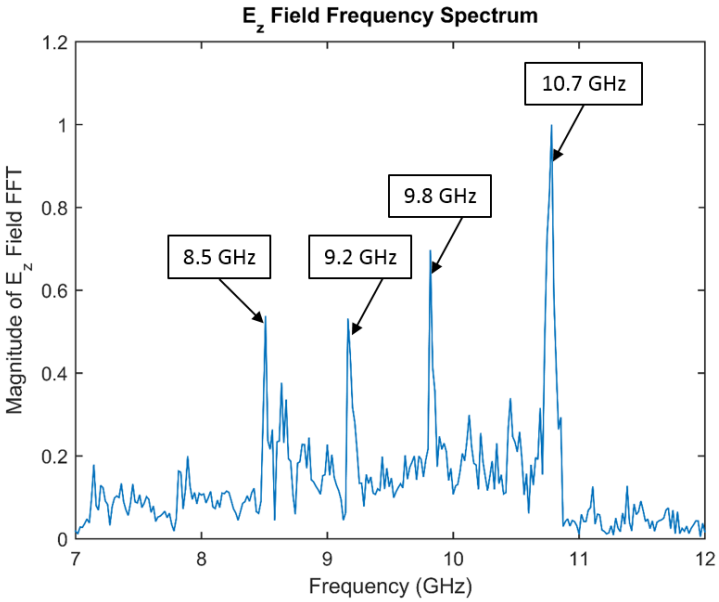

(b)

Figure 4.11: (a)Intensity and (b)FFT of E_z field on the field measurement area for 5 mm d_{ak}.

Table 4.6: A x_{np} value, a cutoff frequency, f_{cutoff} and the main frequency, f_{op} of $TM_{0,12}$, $TM_{0,13}$, $TM_{0,14}$ and $TM_{0,15}$ for $d_{ak} = 5\ mm$.

Mode	x_{np}	f_{cutoff} (GHz)	f_{op} (GHz)
$TM_{0,12}$	36.9171	8.81	8.5
$TM_{0,13}$	40.0584	9.56	9.2
$TM_{0,14}$	43.1998	10.31	9.8
$TM_{0,15}$	46.3412	11.06	10.7

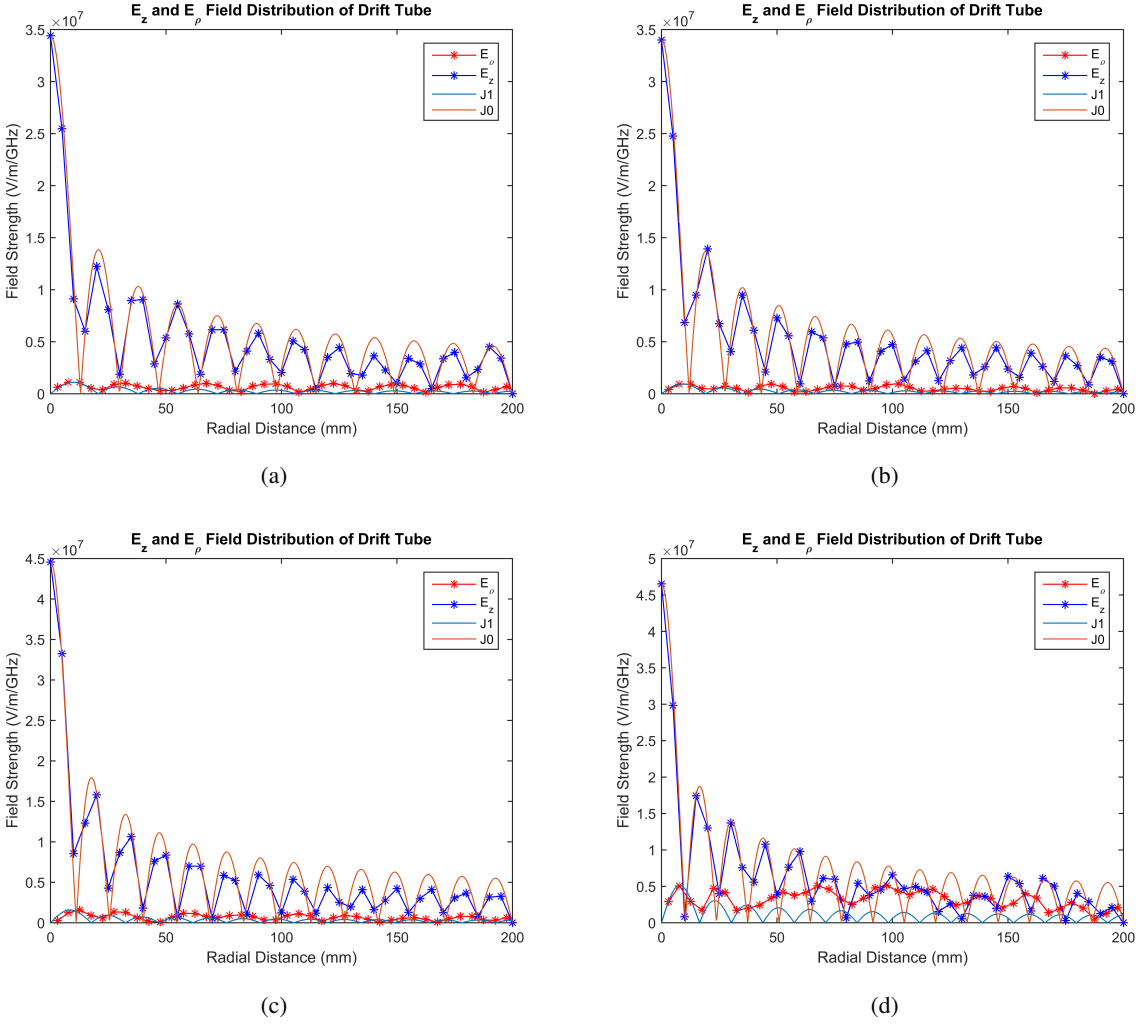

(a) (b)

(c) (d)

Figure 4.12: The radial profile of E field in (a)$TM_{0,12}$ mode at 8.5 GHz (b)$TM_{0,13}$ mode at 9.2 GHz (c)$TM_{0,14}$ mode at 9.8 GHz (d)$TM_{0,15}$ mode at 10.7 GHz for d_{ak}=5 mm.

If special care is not taken regarding the main frequency of the axial vircator and the dimension of the drift tube, a generation of a microwave at a desired single frequency with high efficiency cannot be obtained. As explained in Section 2.7, the mode of the generated microwave is ensured if a radial dimension of the circular waveguide is arranged in ways that the main frequency of the axial vircator is between the cutoff frequencies of TM_{01} and TM_{02}. Thereby, the output mode of the axial vircator can be controlled. In order to demonstrate manageability of the output mode of the axial vircator, it is arranged radius of the circular waveguide as 200 mm and 50 mm for 10 mm d_{ak}. The cross-section view in ρ-z plane for 200 mm and 50 mm radius of the circular waveguide, r_o can be seen in Figure 4.13.

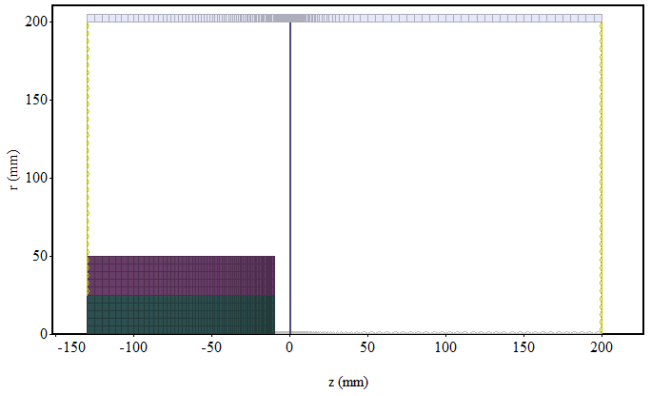

(a)

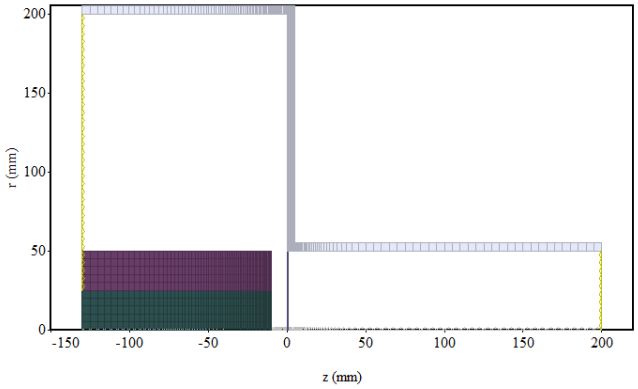

(b)

Figure 4.13: Cross-section in ρ-z plane of the axial vircator with (a)200 mm and (b)50 mm radius of circular waveguide.

The main frequencies of both the axial vircators are calculated as 4.85 GHz by using the same formula in Equation 2.32 and quite close frequency components to the theoretical value are obtained in both simulations. The values of these frequencies can be seen in Figure 4.14 as 4.9 GHz and 4.7 GHz for 200 mm and 50 mm radius of the circular waveguide, respectively.

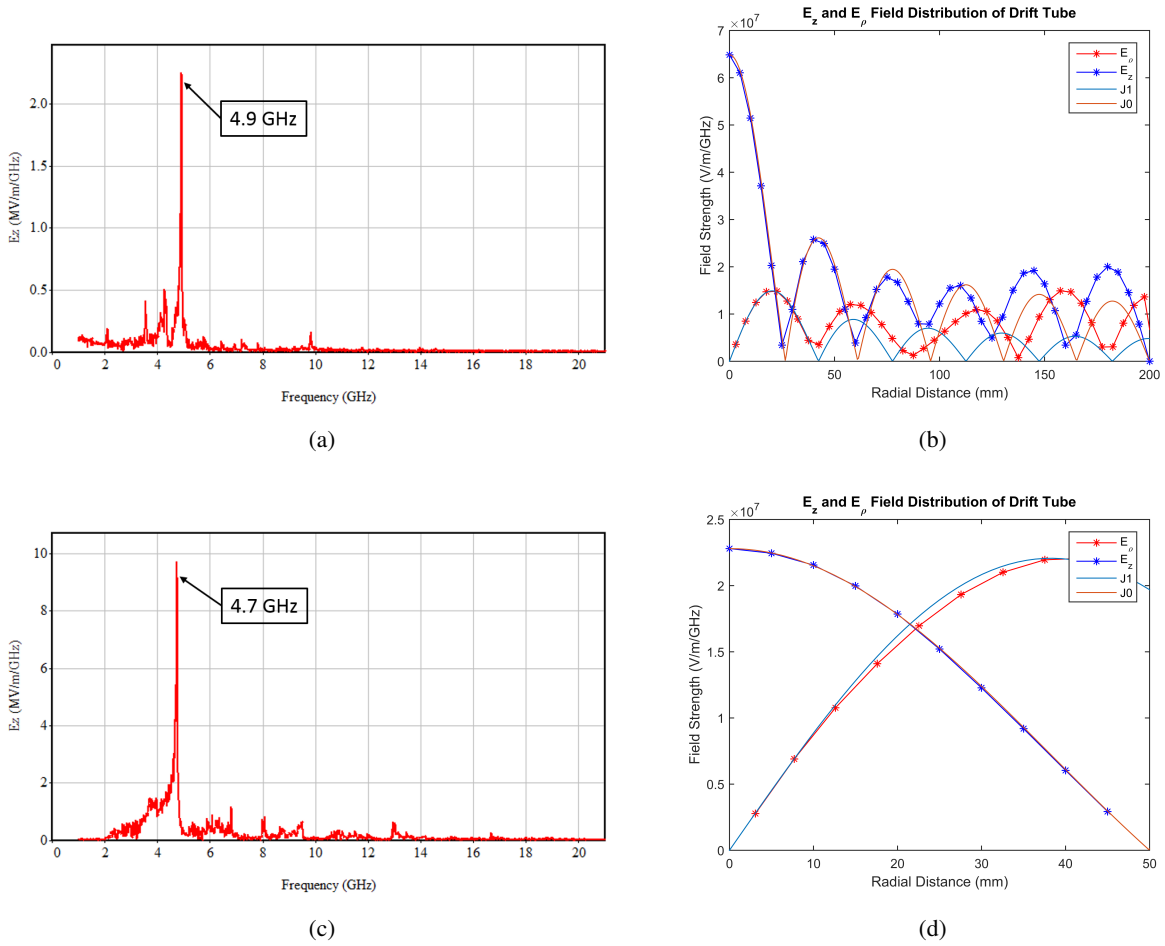

Figure 4.14: (a)FFT of E_z field on the field measurement area and (b)the radial profile of E field in TM_{06} mode at 4.9 GHz for $r_0 = 200\ mm$, (c)FFT of E_z field on the field measurement area and (d)the radial profile of E field in TM_{01} mode at 4.7 GHz for $r_0 = 50\ mm$.

Possible modes of the generated fields are determined as TM_{06} and TM_{01} by calculating cutoff frequencies of each TM_{0n} mode for 200 mm and 50 mm r_0. Then, the radial profiles of E field for each case are fitted the corresponding the Bessel func-

tions, which can be seen these plots in Figure 4.14b and Figure 4.14d. It is clear that TM_{01} mode provides a better consistency as the only possible mode for 50 mm r_0 is nothing short of TM_{01} mode. However, in the case of 200 mm r_0, there could be other modes which share the same frequency component of the field, and it is the inevitable consequence of a negligent selection of the radius of the circular waveguide.

CHAPTER 5

CHARACTERIZATION OF THE INPUT OF THE AXIAL VIRCATOR

Besides enhancing the power conversion efficiency of the vircator, it is significant to optimize the efficiency of all over HPM system, as well. In this regard, to ensure compatibility of the vircator with other elements of the system such as high voltage generator and antenna, gains importance. Hence, characterization of the input port of the vircator provides an opportunity to maximize power delivered to the vircator by the high voltage generator.

Moreover, in the view of vircator itself, a seen voltage at the input of the axial vircator, V_{inlet} is determined by a voltage division between impedances of the high voltage generator and the axial vircator. V_{inlet}, which is directly equal to V_{ak} is of prime importance. It is clear that the main frequency of the vircator, whose formula is given in Equation 2.32 is directly proportional with ${V_{ak}}^{3/2}$. The shift in the main frequency can also affect the power conversion efficiency of the vircator and the mode of the generated microwave. Thus, an operation of the vircator are sensitive to V_{ak}. To conclude, characterization of the input port of the vircator brings flexibility to design the vircator according to system requirements.

5.1 Electrical Model of The Axial Vircator

In [84], axial vircator is modeled with an electrical circuit. The lumped model used in the study is based on modeling of power losses, and so it composes of the resistors. In this approach, the transient characteristics of an input voltage and current are not taken into consideration. However, it is known and measured the inductive behavior of the vircator [56, 85]. The reason can be stated as follows: when the voltage differ-

ence is applied to the input of the axial vircator, there cannot be current emission until the electrical field at the cathode surface reaches its threshold level. After emission of electrons starts, the emitted current due to the electrons and so input current can be observed. In Figure 5.1, measured voltage, V_{inlet} and current, I_{inlet} at the input port of the axial vircator are shown. In the normalized version of these plots, which is given in Figure 5.2, the inductive behavior of the axial vircator can be seen.

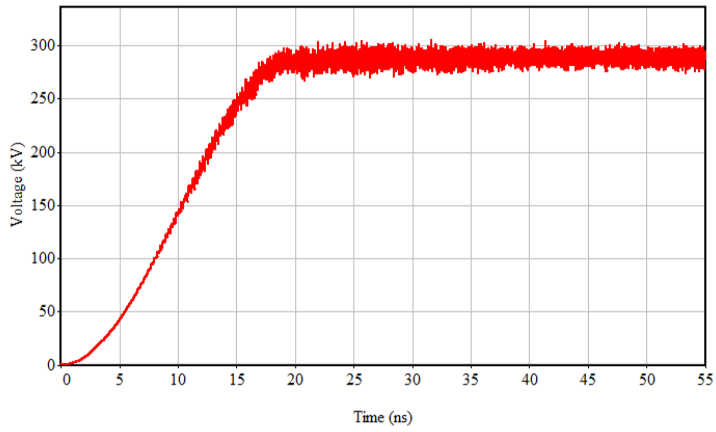

(a)

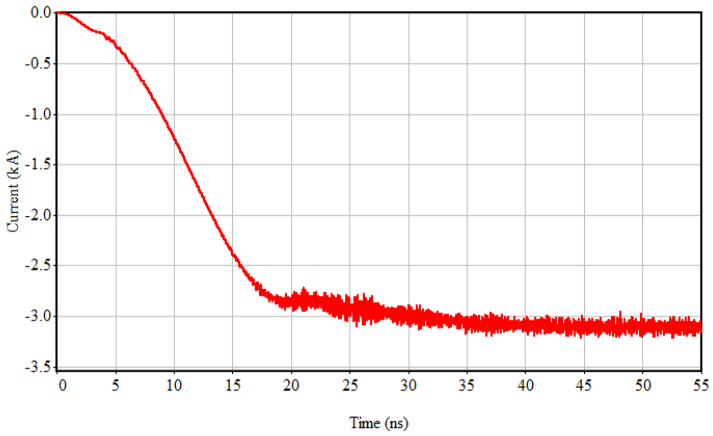

(b)

Figure 5.1: Measured (a)voltage, V_{inlet} and (b)current, I_{inlet} at the input port of the axial vircator for $V_{ak} = 288\ kV$, $d_{ak} = 17\ mm$ and $r_c = 25\ mm$.

The proposed electrical model of the axial vircator is given in Figure 5.3, which is basically composed of serial connected an inductor and a resistor. Since $V_{in}(t)$ is the input of the electrical model, first, the measured voltage, V_{inlet} is written in terms of sum of the ramp functions. Then, by adjusting the values of R_v and L_v, the best fitted

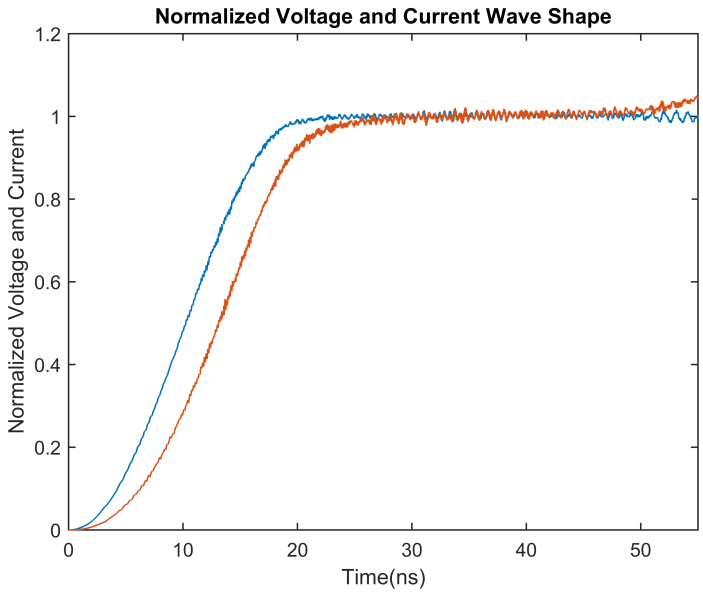

Figure 5.2: Normalized and filtered version of V_{inlet} and I_{inlet} in Figure 5.1.

current $I_{in}(t)$ with the measured current, I_{inlet} is tried to obtain.

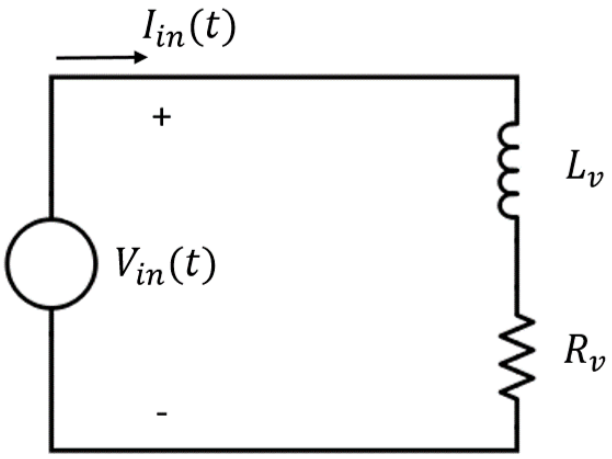

Figure 5.3: Electrical Model of the Axial Vircator.

To drive $I_{in}(t)$ in terms of R_v, L_v and $V_{in}(t)$, Kirchhoff's voltage law should be written as in Equation 5.1.

$$V_{in}(t) = R_v I_{in}(t) + L_v \frac{dI_{in}(t)}{dt} \tag{5.1}$$

Before obtaining expression for the total $I_{in}(t)$, first, a ramp response of the electrical model is derived. Then, the actual response of the circuit will be written by using the superposition principle. Thus, by equating the right hand side of Equation 5.1 to $ramp(t) = t$ for $t > 0$ with $I_{in}(t = 0) = 0$, Equation 5.2 can be obtained.

$$I_{in}(t) = \frac{L_v}{{R_v}^2}\left(e^{-\frac{t}{\tau}} - 1\right) + \frac{t}{R_v} \tag{5.2}$$

where $\tau = \frac{L_v}{R_v}$. Now, $V_{in}(t)$ can be written in the form, which is given in Equation 5.3.

$$V_{in}(t) = \frac{V_{max}}{t_2 - t_1}(ramp(t - t_1) - ramp(t - t_2)) \tag{5.3}$$

where t_1 and t_2 are the parameters which are used in order to tune theoretical $V_{in}(t)$ to the measured V_{inlet}. Their values are $3.45\ ns$ and $16.75\ ns$, respectively.
Then, for $V_{in}(t)$ given in Equation 5.3, $I_{in}(t)$ is found as follows:

$$I_{in}(t) = \frac{V_{max}}{t_2 - t_1}\left(\frac{L_v}{{R_v}^2}\left(e^{-\frac{t-t_1}{\tau}} - e^{-\frac{t-t_2}{\tau}}\right) + \frac{t_2 - t_1}{R_v}\right) \tag{5.4}$$

The fitted voltage $V_{in}(t)$ with V_{inlet} and its response $I_{in}(t)$ with I_{inlet} of the simulation whose measured graphs are given in Figure 5.1 can be seen in Figure 5.4. When the fitting both voltage and current graphs, it is paid attention to equalize the steady-state top value and the rising slops of both waveforms.

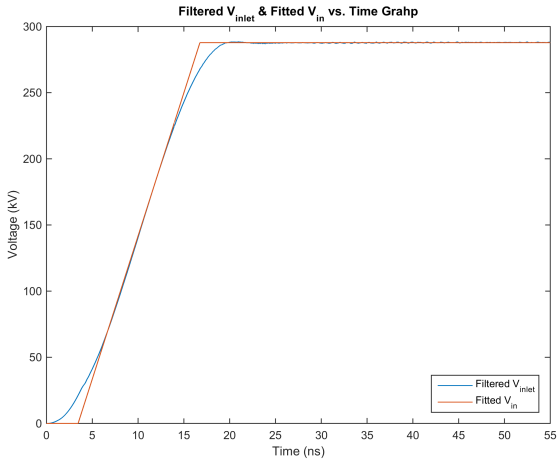

(a)

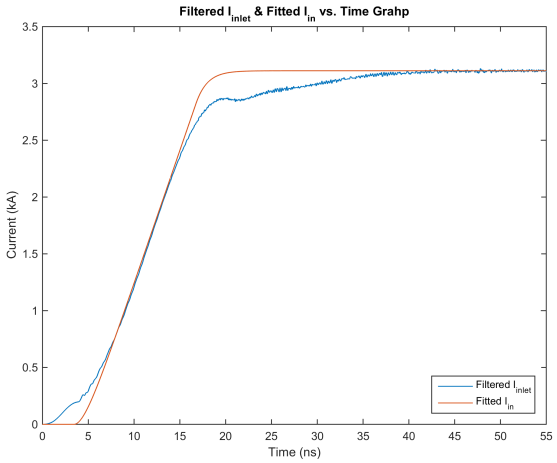

(b)

Figure 5.4: Fitted (a)voltage, V_{in} and (b)current, I_{in} at the input port of the axial vircator for $V_{ak} = 288\ kV$, $d_{ak} = 17\ mm$ and $r_c = 25\ mm$.

For several values of three different vircator's parameters, which are V_{ak}, r_c and d_{ak}, R_v and L_v values of the equivalent electrical model of the axial vircator are found.It is beneficial to note that all the measured and fitted graphs of voltage and current for these simulations are given in Appendix A. Moreover, for each simulation, it is observed the diamond shape in the phase space diagram, which means that the vircator forms the virtual cathode and can properly operate as expected.

5.1.1 Sweep of The Applied Voltage

The simulations whose fitted voltage and current graphs are given in Figure A.1 have $r_c = 25\ mm$ and $d_{ak} = 17\ mm$. V_{ak} is swept in non-relativistic case, which implies that the applied voltage is smaller than $500\ kV$. The values of the applied voltage is given in Table 5.1. In this table, the obtained values of L_v and R_v are listed. It is clearly seen that change in V_{ak} does not have any effect on acquired L_v values.

Table 5.1: Obtained parameters L_v and R_v of the proposed electrical model of the axial vircator for different V_{ak} values.

V_{ak} (kV)	L_v (nH)	R_v (Ω)
100	140	155
200	140	106
288	140	93
400	140	80
500	140	75

The variation on R_v values for V_{ak} is plotted in Figure 5.5.

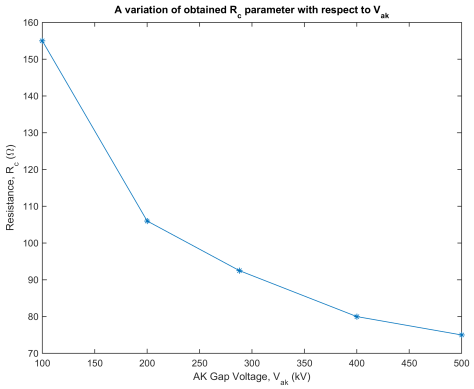

Figure 5.5: A variation on the obtained R_c parameter for V_{ak}.

5.1.2 Sweep of The Cathode Radius

The simulations whose fitted voltage and current graphs are given in Figure A.2 have $V_{max} = 288\ kV$ and $d_{ak} = 17\ mm$. The parameter r_c is swept from $135\ mm$ to $20\ mm$. Relatively larger cathode radiuses, r_c result with the more smooth fitting. The inverse relation between the cathode radius, r_c and the obtained L_v and R_v is seen in Figure 5.6. The values of these parameters are listed in Table 5.2, as well.

Table 5.2: Obtained parameters L_v and R_v of the proposed electrical model of the axial vircator for different r_c values.

r_c (mm)	L_v (nH)	R_v (Ω)
135	8	11.8
85	22	21.2
45	60	47.0
40	70	54.0
35	80	60.0
30	90	74.0
25	140	92.5
20	160	122.0

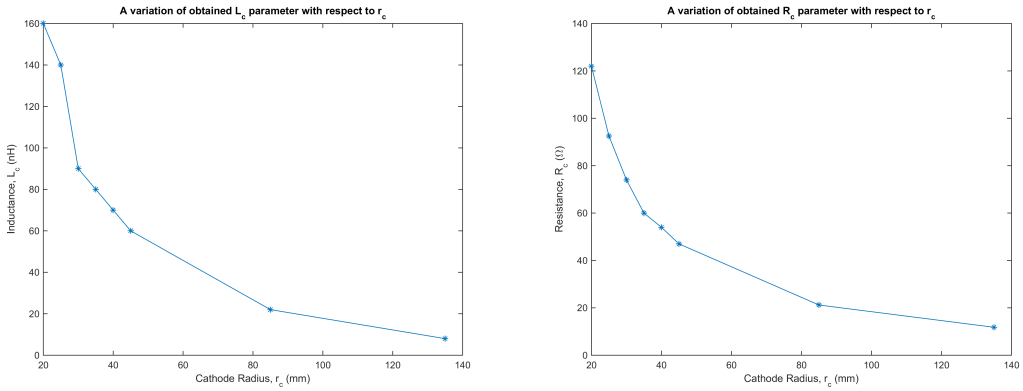

(a) (b)

Figure 5.6: A variation on the obtained (a)L_v and (b)R_c parameter for r_c.

5.1.3 Sweep of The AK Gap Separation

The simulations whose fitted voltage and current graphs are given in Figure A.3 have $V_{max} = 288\ kV$ and $r_c = 25\ mm$. The most accurate fittings are obtained for the smaller d_{ak} values. Moreover, in contrast to the cathode radius, r_c, d_{ak} has direct proportion with the obtained L_v and R_v values. The variation of the inductance L_v and the resistance R_v are given in Figure 5.7. The values of the predicted components are given in Table 5.3.

Table 5.3: Obtained parameters L_v and R_v of the proposed electrical model of the axial vircator for different d_{ak} values.

d_{ak} (mm)	L_v (nH)	R_v (Ω)
5	60	19.85
10	100	45.50
15	130	76.50
17	140	92.50
20	150	116.00

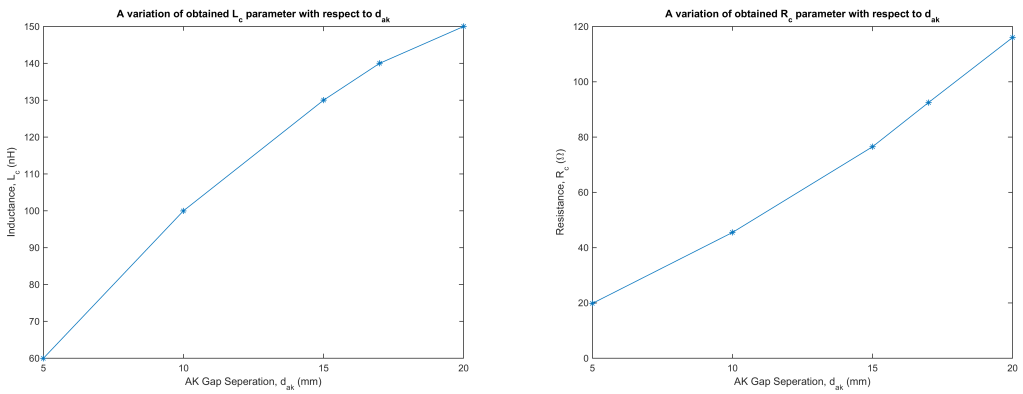

(a) (b)

Figure 5.7: A variation on the obtained (a)L_v and (b)R_c parameter for d_{ak}.

5.1.4 Conclusion

In this chapter, the electrical model of the axial vircator is proposed. Then, a variation of the components' values in the proposed electrical model by V_{ak}, r_c and d_{ak} is examined. Although some studies exist regarding the modeling of the axial vircator's input, a parametric study on the input characterization of the axial vircator by using its transient characteristics is the first in literature. Hence, this claim and findings are required to be validated by experimental results, as well. After verification of the suggested model, it can be used in designing the axial vircator according to system requirements with satisfying the optimum total efficiency.

CHAPTER 6

CONCLUSION AND FUTURE WORK

6.1 Conclusion

Vircator is one of the HPM sources which is widely studied and discussed since its first invention. Due to vircator's relatively simple structure and operation principles, the analytical formulation efforts of the generation of the relativistic electron beam and its interaction with electromagnetic fields is more attractive compared to other HPM sources like BWO, relativistic magnetron, etc. In the design efforts, most of the studies are aimed to enhance the power conversion efficiency of the vircator.

In order to comprehend the basis of the vircator, it is preferred to focus on the most basic but nevertheless, the essential type of the vircator named the axial vircator. Considering these facts, axial vircator structure is studied in this thesis. The main objective of this thesis is to investigate the axial vircator in several aspects to digest the fundamentals of its operation.

In Chapter 2, the essential concepts for the vircator are introduced. Moreover, two critical currents for the vircator, which are the one-dimensional Child-Langmuir law for current and the space charge limiting current are derived. In formulations, due to the complexity of the interactions, basic assumptions lead to close form expressions, which are not practically valid. Simulation-based empirical approaches are developed in the literature. The extensions to the two-dimensional structure with two different approaches, which are uniform and non-uniform current density, are also introduced and examined.

Presence of moving electrons creates an electromagnetic problem with the presence

of the source. Conventionally in most of the electromagnetic problems, like antenna design, source free media are elaborated. This difference necessitates the introduction of the PIC (particle in cell) code. Numerous work on HPM devices and systems are based on the simulation results of these codes. In Chapter 3, general information about the employed simulation environment, Magic 3D is given. All arrangements for vircator in simulation environment are explained.

The cathode of the vircator, just like the cathodes of other HPM sources, is one of the most critical parts in the design and implementation of the device. The generation of the electron beam at the cathode is the starting point for the microwave generation. For an analytical understanding of the behavior and also for optimizing the performance (such as efficiency), the correct form of the electron beam should be achieved. In Chapter 4, the effects of introducing the cathode ring on the formation of the desired electron beam are examined. The optimum length for the cathode ring is determined regarding the emitted current and the efficiency of the axial vircator. Then, two critical currents of the axial vircator are mainly discussed. It is shown that the excess of the reflected electrons' existence due to to $I_{SCL} << I_{emit}$ condition causes the modulation of the electron beam in the diode region. After, the claim of the relation between the disturbance of the electron beam and the emitting current's being lower than even the 1D CL current is asserted.

Furthermore, the effect of this excessive reflexing current on the efficiency of the axial vircator is demonstrated. It is understood that the case of the domination of the reflected electron emission provides the output power with relatively higher efficiency. Hence, it is concluded that in order to achieve microwave output with a higher order of magnitude, the microwave generation mechanism of the reflexing electrons should dominate the process. Moreover, it is observed that one of the main factors of the efficiency drop is frequency splitting and so mode competition by identifying modes of the generated microwave. In addition to that, the more agreeable mode fitting is obtained TM_{01} mode, which is the lowest mode of TM_{0n} when compared to the higher order of TM_{0n} mode for the almost same frequency. The generation of the TM_{01} mode is guaranteed by adjusting the radius of the drift tube properly.

The overall HPM system consists of the high voltage source and the microwave device

(i.e., the vircator in this case) together with all other parts like the mode converter, antenna and the pulse forming line. As known from the electrical engineering aspects, optimization of the source load interaction has a certain influence on the efficiency of the energy transfer. Since the weakest point of the vircator is its efficiency, optimizing the high voltage source – vircator interaction is a natural remedy. For this purpose, input characteristic of the axial vircator is studied. In Chapter 5, the electrical equivalent circuit of the axial vircator is proposed. This circuit mainly composes of resistive R_c and L_c. The change of these circuit parameters with respect to the axial vircator's parameters which are V_{ak}, d_{ak} and r_c are studied. In literature, although there are several studies concerning modeling input of the vircator with lumped elements, a parametric study of the input port of the axial vircator cannot be made. Hence, it is required to support these part of the thesis with the experimental study.

To conclude, the axial vircator is widely discussed in this thesis. The analysis and characterization of this structure are made in many aspects. With this thesis work, it is shown that the excess of the reflected electrons' existence causes the modulation of electron flow in the diode region, which results in the decrease on the emitting current from its theoretical value. Moreover, it is emphasized that the domination of the reflexing electrons also affects the efficiency of the axial vircator. Finally, the suggested electrical circuit for the input of the axial vircator and the variation of the values of its components with respect to the parameters of the vircator are investigated in this thesis.

6.2 Future Work

Based on the studies in this thesis, other types of the vircator can be examined to enhance the power conversion efficiency of the vircator. Moreover, it might be possible to make some modifications in an existing structure in order to increase the efficiency by promoting electrons for reflexing motion.

Furthermore, by manufacturing the studied axial vircator structure, a fabrication experience of the vacuum tube can be gained. Moreover, by producing the axial vircator, tests and calibrations for HPM measurement setup can be readily utilized.

REFERENCES

[1] J. Benford, J. A. Swegle, and E. Schamiloglu, *High power microwaves, 3rd ed.* CRC Press, third edit ed., 2016.

[2] V. Kesari and B. N. Basu, *High power microwave tubes: basics and trends volume 1*. Morgan & Claypool Publishers, 2018.

[3] V. L. Granatstein and I. Alexeff, *High-power microwave sources*. Norwood: Artech House, 1987.

[4] C. D. Child, "Discharge from hot cao," *Physical Review (Series I)*, vol. 32, no. 5, pp. 492–511, 1911.

[5] I. Langmuir, "The effect of space charge and resdual gases on thermionic currents in high vacuum," *Physical Review*, vol. 2, no. 6, pp. 450–486, 1913.

[6] R. A. Mahaffey, P. Sprangle, J. Golden, and C. A. Kapetanakos, "High-power microwaves from a nonisochronic reflecting electron system," *Physical Review Letters*, vol. 39, no. 13, 1977.

[7] D. J. Sullivan, "Applications of the virtual cathode in relativistic electron beams," in *3rd International Topical Conference on High-Power Electron and Ion Beam Research & Technology*, pp. 769–772, 1979.

[8] J. M. Buzzi, H. J. Doucet, B. Etlicher, P. Haldenwang, A. Huetz, H. Lamain, C. Rouille, J. Cabe, J. Belvaux, J. C. Jouys, and C. Peugnet, "Microwave generation and frequency conversion using intense relativistic electron beams," in *2nd International Topical Conference on High Power Electron and Ion Beam Research & Technology*, 1977.

[9] J. Benford, D. Price, H. Sze, D. Bromley, J. Benford, D. Price, H. Sze, and D. Bromley, "Interaction of a vircator microwave generator with an enclosing resonant cavity," *Journal of Applied Physics*, vol. 61, no. 5, pp. 2098–2010, 1987.

[10] T. J. T. Kwan, D. Fulton, and G. Sherwood, "Theoretical and experimental investigation of reditrons," in *SPIE*, pp. 62–67, 1988.

[11] P. Poulsen, P. A. Pincosy, and J. J. Morrison, "Progress toward steady-state, high-efficiency vircators," in *SPIE*, vol. 1407, pp. 172–182, 1991.

[12] K. Woolverton, M. Kristiansen, and L. L. Hatfield, "Computer simulations of coaxial vircators," *SPIE*, vol. 3158, pp. 145–152, 1997.

[13] W. Jiang, "High power microwave generation by a coaxial vircator," in *13th International Conference on High-Power Particle Beams*, 2000.

[14] S. A. Kitsanov, A. I. Klimov, S. D. Korovin, I. K. Kurkan, I. V. Pegel, and S. D. Polevin, "A vircator with electron beam premodulation based on high-current repetitively pulsed accelerator," *IEEE Transactions on Plasma Science*, vol. 30, no. 1, pp. 274–285, 2002.

[15] W. Jeon, J. E. Lim, M. W. Moon, K. B. Jung, W. B. Park, H. M. Shin, and Y. Seo, "Output characteristics of the high-power microwave generated from a coaxial vircator with a bar reflector in a drift region," *IEEE Transactions on Plasma Science*, vol. 34, no. 3, pp. 937–944, 2006.

[16] Z. Li, H. H. Zhong, Y. Fan, T. Shu, J. H. Yang, C. W. Yuan, L. R. Xu, and Y. Zhao, "Simulation and experimental research of a novel vircator," *Chinese Physics Letters*, vol. 25, no. 7, pp. 2566–2568, 2008.

[17] S. Champeaux, P. Gouard, R. Cousin, and J. Larour, "Improved design of a multistage axial vircator with reflectors for enhanced performances," *IEEE Transactions on Plasma Science*, vol. 44, no. 1, pp. 31–38, 2016.

[18] C. Möller, *Design and experiments with high power microwave sources*. PhD thesis, KTH, 2012.

[19] S. Humphries, *Charged particle beams*. 2002.

[20] S. Champeaux, P. Gouard, R. Cousin, and J. Larour, "3-D PIC numerical investigations of a novel concept of multistage axial vircator for enhanced microwave generation," *IEEE Transactions on Plasma Science*, vol. 43, no. 11, pp. 3841–3855, 2015.

[21] M. Haworth, R. Adler, B. Anderson, M. Connaughton, W. Dungan, J. Enns, J. Metz, P. Pelletier, R. Platt, J. Polaco, R. Rupp, L. Thode, and D. Voss, "Experimental observation of two microwave radiation mechanisms with widely separated frequencies during the output pulse of a high-voltage virtual cathode oscillator," *Applied Physics Letters*, vol. 59, no. 4, pp. 408–410, 1991.

[22] M. Hägg, *Theoretical analysis and simulation of microwave-generation from a coaxial vircator*. PhD thesis, Uppsala University, 2017.

[23] D. J. Sullivan, "High power microwave generation from a virtual cathode oscillator (vircator)," *IEEE Transactions on Nuclear Science*, vol. NS-30, no. 4, pp. 3426–3428, 1983.

[24] T. J. T. Kwan, "High-power coherent microwave generation from oscillating virtual cathodes," *Physics of Fluids*, vol. 27, no. 1, pp. 228–232, 1984.

[25] W. Jiang, K. Masugata, and K. Yatsui, "Mechanism of microwave generation by virtual cathode oscillation," *Physics of Plasmas*, vol. 2, no. 3, pp. 982–986, 1995.

[26] V. Kesari and B. N. Basu, *High power microwave tubes: basics and trends volume 2*. Morgan & Claypool Publishers, 2018.

[27] R. B. Miller, *An introduction to the physics of intense charged particle beams*. Plenum Press, 1982.

[28] R. K. Parker, R. E. Anderson, and C. V. Duncan, "Plasmainduced field emission and the characteristics of highcurrent relativistic electron flow," *Journal of Applied Physics*, vol. 45, no. 6, pp. 2463–2479, 1974.

[29] D. T. Young, *Effects of diode gap closure and bipolar flow on vircator microwave generation*. PhD thesis, Texas Tech University, 1996.

[30] J. Petrén, *Frequency tunability of axial cavity vircators and double anode vircators Frequency tunability of axial cavity vircators and double anode vircators*. PhD thesis, KTH Royal Institute of Technology, 2016.

[31] M. Yatsuzuka, M. Nakayama, and M. Tanigawa, "Plasma effects on electron

beam focusing and microwave emission in a virtual cathode oscillator," *IEEE Transactions on Plasma Science*, vol. 26, no. 4, pp. 1314–1321, 1998.

[32] L. Li, G. Cheng, L. Zhang, X. Ji, L. Chang, Q. Xu, L. Liu, J. Wen, and C. Li, "Role of the rise rate of beam current in the microwave radiation of vircator," *Journal of Applied Physics*, vol. 109, no. 074504, 2011.

[33] D. Shiffler, M. LaCour, M. Sena, M. Mitchell, M. Haworth, K. Hendricks, and T. Spencer, "Comparison of carbon fiber and cesium iodide-coated carbon fiber cathodes," *IEEE Transactions on Plasma Science*, vol. 28, no. 3, pp. 517–522, 2000.

[34] D. Shiffler, M. Ruebush, M. LaCour, K. Golby, R. J. Umstattd, M. C. Clark, J. W. Luginsland, D. Zagar, and M. Sena, "Emission uniformity and emission area of explosive field emission cathodes," *Applied Physics Letters*, vol. 79, no. 18, pp. 2871–2873, 2001.

[35] D. Shiffler, M. LaCour, K. Golby, M. Sena, M. Mitchell, M. Haworth, K. Hendricks, and T. Spencer, "Comparison of velvet- and cesium iodide-coated carbon fiber cathodes," *IEEE Transactions on Plasma Science*, vol. 29, no. 3, pp. 445–451, 2001.

[36] D. Shiffler, M. Ruebush, D. Zagar, M. Lacour, M. Sena, K. Golby, M. Haworth, and R. J. Umstattd, "Cathode and anode plasmas in short-pulse explosive field emission cathodes," *Journal of Applied Physics*, vol. 91, no. 9, pp. 5599–5603, 2002.

[37] Y. Chen, J. Mankowski, J. Walter, M. Kristiansen, and R. Gale, "Cathode and anode optimization in a virtual cathode oscillator *," *IEEE Transactions on Dielectrics and Electrical Insulation*, vol. 14, no. 4, pp. 1037–1044, 2007.

[38] J. Benford and G. Benford, "Survey of pulse shortening in high-power microwave sources," *IEEE Transactions on Plasma Science*, vol. 25, no. 2, pp. 311–317, 1997.

[39] A. Roy, A. Patel, R. Menon, A. Sharma, D. P. Chakravarthy, and D. S. Patil, "Emission properties of explosive field emission cathodes," *Physics of Plasmas*, vol. 18, no. 10, 2011.

[40] P. Zhang, Á. Valfells, L. K. Ang, J. W. Luginsland, and Y. Y. Lau, "100 years of the physics of diodes," *Applied Physics Reviews*, vol. 4, no. 1, 2017.

[41] Y. E. Krasik, A. Dunaevsky, A. Krokhmal, J. Felsteiner, A. V. Gunin, Y. E. Krasik, A. Dunaevsky, A. Krokhmal, and J. Felsteiner, "Emission properties of different cathodes at E105V / cm," *Journal of Applied Physics*, vol. 89, no. 4, pp. 2379–2399, 2001.

[42] M. Elfsberg, T. Hurtig, A. Larsson, C. Möller, and S. E. Nyholm, "Experimental studies of anode and cathode materials in a repetitive driven axial vircator," *IEEE Transactions on Plasma Science*, vol. 36, no. 3, pp. 688–693, 2008.

[43] K. I. Frank Stephens, *Space-charge saturation and current limits in cylindrical*. PhD thesis, University of North Texas, 2000.

[44] C. Möller, M. Elfsberg, A. Larsson, and S. E. Nyholm, "Experimental studies of the influence of a resonance cavity in an axial vircator," *IEEE Transactions on Plasma Science*, vol. 38, no. 6 PART 1, pp. 1318–1324, 2010.

[45] J. W. Luginsland, Y. Y. Lau, and R. M. Gilgenbach, "Two-dimensional Child-Langmuir law," *Physical Review Letters*, vol. 77, no. 22, pp. 4668–4670, 1996.

[46] Y. Y. Lau, "Simple theory for the two-dimensional Child-Langmuir law," *Physical Review Letters*, vol. 87, no. 27, p. 278301, 2001.

[47] J. W. Luginsland, Y. Y. Lau, R. J. Umstattd, and J. J. Watrous, "Beyond the Child-Langmuir law: a review of recent results on multidimensional space-charge-limited flow," *Physics of Plasmas*, vol. 9, no. 5, pp. 2371–2376, 2002.

[48] W. S. Koh, L. K. Ang, and T. J. T. Kwan, "Three-dimensional Child-Langmuir law for uniform hot electron emission," *Physics of Plasmas*, vol. 12, no. 5, pp. 1–6, 2005.

[49] R. Miller, Y. Y. Lau, and J. H. Booske, "Electric field distribution on knife-edge field emitters," *Applied Physics Letters*, vol. 91, no. 7, pp. 17–20, 2007.

[50] R. Miller, Y. Y. Lau, and J. H. Booske, "Schottky's conjecture on multiplication of field enhancement factors," *Journal of Applied Physics*, vol. 106, no. 10, 2009.

[51] R. J. Umstattd and J. W. Luginsland, "Two-dimensional space-charge-limited emission: Beam-edge characteristics and applications," *Physical Review Letters*, vol. 87, no. 14, pp. 1–4, 2001.

[52] J. J. Watrous, J. W. Luginsland, and M. H. Frese, "Current and current density of a finite-width, space-charge-limited electron beam in two-dimensional, parallel-plate geometry," *Physics of Plasmas*, vol. 8, no. 9, pp. 4202–4210, 2001.

[53] A. Rokhlenko and J. L. Lebowitz, "Space-charge-limited 2D electron flow between two flat electrodes in a strong magnetic field," *Physical Review Letters*, vol. 91, no. 8, p. 085002, 2003.

[54] L. S. Bogdankevich and A. A. Rukhadze, "Stability of relativistic electron beams in a plasma and the problem of critical currents," *Soviet Physics Uspekhi*, vol. 14, no. 2, pp. 163–179, 1971.

[55] T. J. T. Kwan and L. E. Thode, "Formation of virtual cathodes and microwave generation in relativistic electron beams," *Physics of Fluids*, vol. 27, no. 7, pp. 1570–1572, 1984.

[56] E. H. Choi, M. C. Choi, Y. Jung, M. W. Chong, J. J. Ko, Y. Seo, G. Cho, H. S. Uhm, and H. Suk, "High-power microwave generation from an axially extracted virtual cathode oscillator," *IEEE Transactions on Plasma Science*, vol. 28, no. 6, pp. 2128–2134, 2000.

[57] S. C. Burkhart, R. D. Scarpetti, and R. L. Lundberg, "A virtual-cathode reflex triode for high-power microwave generation," *Journal of Applied Physics*, vol. 58, no. 1, pp. 28–36, 1985.

[58] H. Sze, J. Benford, T. Young, D. Bromley, and B. Harteneck, "A radially and axially extracted virtual-cathode oscillator (vircator)," *IEEE Transactions on Nuclear Science*, vol. 13, no. 6, pp. 492–497, 1985.

[59] W. Jiang, K. Woolverton, J. Dickens, and M. Kristiansen, "High power microwave generation by a coaxial virtual cathode oscillator," *IEEE Transactions on Plasma Science*, vol. 27, no. 5, pp. 1538–1542, 1999.

[60] D. Biswas and R. Kumar, "Efficiency enhancement of the axial vircator," *IEEE Transactions on Plasma Science*, vol. 35, no. 2 III, pp. 369–378, 2007.

[61] G. R. Turner and G. R. Turner, "A one-dimensional model illustrating virtual-cathode formation in a novel coaxial virtual-cathode oscillator," *Physics of Plasmas*, vol. 21, no. 093104, pp. 1–9, 2014.

[62] K. B. Song, J. E. Lim, Y. Seo, and E. H. Choi, "Output characteristics of the axially extracted virtual cathode oscillator with a cathode-wing," *IEEE Transactions on Plasma Science*, vol. 37, no. 2, pp. 304–310, 2009.

[63] K. R. Clements, *Design and experimental study of a dual vircator microwave source*. PhD thesis, University of Missouri-Columbia, 2012.

[64] W.-Y. Woo, "Two-dimensional features of virtual cathode and microwave emission," *Physics of Fluids*, vol. 30, no. 1, pp. 239–244, 1987.

[65] H. Sze, J. Benford, W. Woo, and B. Harteneck, "Dynamics of a virtual cathode oscillator driven by a pinched diode," *Physics of Fluids*, vol. 29, no. 11, pp. 3873–3880, 1986.

[66] C. S. Hwang, M. W. Wu, P. S. Song, and W. S. Hou, "High power microwave generation from a tunable radially extracted vircator," *Journal of Applied Physics*, vol. 69, no. 3, pp. 1247–1252, 1991.

[67] G. Singh and S. Chaturvedi, "PIC simulation of effect of energy-dependent foil transparency in an axially-extracted vircator," *IEEE Transactions on Plasma Science*, vol. 32, pp. 2210–2216, dec 2004.

[68] G. Singh and M. V. Kartikeyan, "Feasibility study of axially- extracted virtual cathode oscillator," *International Journal of Infrared and Millimeter Waves*, vol. 28, no. 11, pp. 911–922, 2007.

[69] R. D. Scarpetti and S. C. Burkhart, "The study of a reflex oscillator used to generate high-power microwaves," *IEEE Transactions on Plasma Science*, vol. 13, no. 6, pp. 506–512, 1985.

[70] A. L. Peratt, C. M. Snell, and L. E. Thode, "A high-power reflex triode microwave source," *IEEE Transactions on Plasma Science*, vol. PS-13, no. 6, pp. 498–505, 1985.

[71] A. Chittora, J. Mukherjee, S. Singh, and A. Sharma, "Dielectric loaded TM01 to TE11 mode converter for S-band applications," *IEEE Transactions on Dielectrics and Electrical Insulation*, vol. 22, no. 4, pp. 2057–2063, 2015.

[72] A. Chittora, S. Singh, A. Sharma, and J. Mukherjee, "A tapered metallic baffle TM01 to TE11y mode converter with TE11x mode transmission capabiliry," *IEEE Microwave and Wireless Components Letters*, vol. 25, no. 10, pp. 633–635, 2015.

[73] A. Chittora, S. Singh, A. Sharma, and J. Mukherjee, "A Novel TM01 to TE11 mode converter designed with radially loaded dielectric slabs," *IEEE Transactions on Microwave Theory and Techniques*, vol. 64, no. 4, pp. 1170–1175, 2016.

[74] A. Chittora, S. Singh, A. Sharma, and J. Mukherjee, "A TM01 to TE11 mode converter designed with semicircular waveguide sections," in *2017 11th European Conference on Antennas and Propagation (EUCAP)*, pp. 1903–1906, 2017.

[75] A. Patri and A. Chittora, "Compact TM01 toTE11 mode converter designed with matching sections," in *2017 IEEE International Symposium on Antennas and Propagation & USNC/URSI National Radio Science Meeting*, pp. 2217–2218, 2017.

[76] L. Ludeking, A. Woods, and L. Cavey, "MAGIC 3.2.0 help Manuel," 2011.

[77] B. Goplen, L. Ludeking, D. Smith, and G. Warren, "User-configurable MAGIC for electromagnetic PIC calculations," *Computer Physics Communications*, vol. 87, pp. 54–86, 1995.

[78] L. Liu, L. Li, X. P. Zhang, J. Wen, H. Wan, and Y. Z. Zhang, "Efficiency enhancement of reflex triode virtual cathode oscillator using the carbon fiber cathode," *IEEE Transactions on Plasma Science*, vol. 35, no. 2, pp. 361–368, 2007.

[79] F. Hegeler, M. Friedman, M. C. Myers, J. D. Sethian, and S. B. Swanekamp, "Reduction of edge emission in electron beam diodes," *Physics of Plasmas*, vol. 9, no. 10, pp. 4309–4315, 2002.

[80] A. Roy, A. Sharma, S. Mitra, R. Menon, V. Sharma, K. V. Nagesh, and D. P. Chakravarthy, "Oscillation frequency of a reflex-triode virtual cathode oscillator," *IEEE Transactions on Electron Devices*, vol. 58, pp. 553–561, feb 2011.

[81] W. Yang and W. Ding, "Studies on a new dual-coaxial vircator," *IEEE Transactions on Plasma Science*, vol. 32, no. 3, pp. 1187–1190, 2004.

[82] A. L. Peratt, M. A. Mostrom, T. J. T. Kwan, and L. E. Thode, "Pulsed-power diode generation of high-power microwaves," in *International Conference on High-Power Particle Beams*, 1983.

[83] J. W. Luginsland, S. McGee, and Y. Y. Lau, "Virtual cathode formation due to electromagnetic transients," *IEEE Transactions on Plasma Science*, vol. 26, no. 3, pp. 901–904, 1998.

[84] K. A. Lee and K. C. Ko, "Electrical circuit modeling for efficiency improvement of axial virtual cathode oscillator," *IEEE Transactions on Plasma Science*, vol. 42, no. 10, pp. 3295–3298, 2014.

[85] E. H. Choi, K. Sung, W. Jeon, and Y. Jung, "Axially extracted virtual cathode oscillator with an annular cathode for enhancement of the microwave conversion efficiency," *Journal of the Korean Physical Society*, vol. 44, no. 5, pp. 1256–1260, 2004.

APPENDIX A

APPENDIX A

First of all, it can be noted that all measured voltage, V_{inlet} and current,I_{inlet} plots which are used to fit the theoretical ones $V_{in}(t)$ and $I_{in}(t)$ are filtered to satisfy more precise fitting. As indicated in each figure, blue plots belong to measured and then filtered V_{inlet} and I_{inlet}, whereas plots with orange color show theoretically found $V_{in}(t)$ and $I_{in}(t)$.

In Figure A.1, the simulations whose fitted voltage and current graphs are given have $r_c = 25\ mm$ and $d_{ak} = 17\ mm$. In Figure A.2, the simulations whose fitted voltage and current graphs are given, have $V_{max} = 288\ kV$ and $d_{ak} = 17\ mm$. In Figure A.3, the simulations whose fitted voltage and current graphs are given, have $V_{max} = 288\ kV$ and $r_c = 25\ mm$.

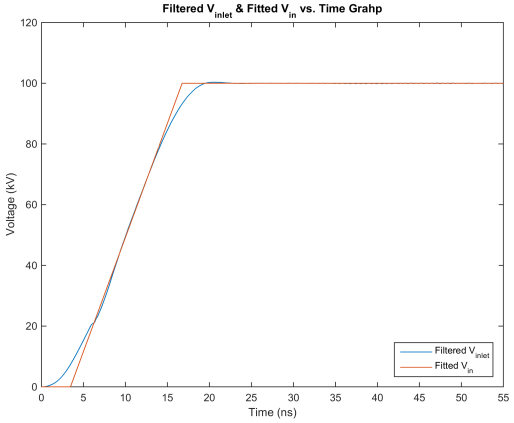
Filtered V_{inlet} & Fitted V_{in} vs. Time Grahp
Voltage (kV)
Time (ns)
Filtered V_{inlet}
Fitted V_{in}

(a)

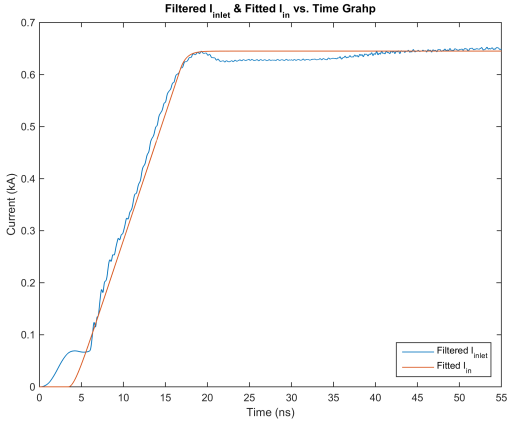
Filtered I_{inlet} & Fitted I_{in} vs. Time Grahp
Current (kA)
Time (ns)
Filtered I_{inlet}
Fitted I_{in}

(b)

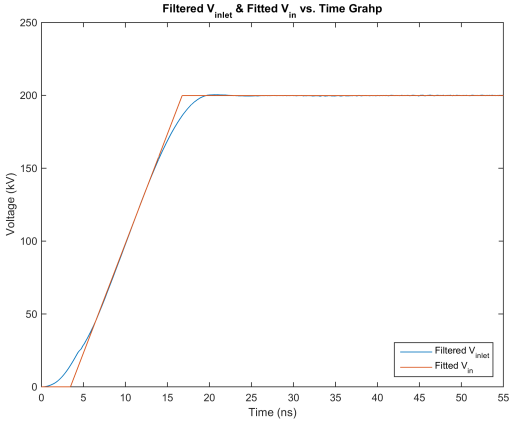
Filtered V_{inlet} & Fitted V_{in} vs. Time Grahp
Voltage (kV)
Time (ns)
Filtered V_{inlet}
Fitted V_{in}

(c)

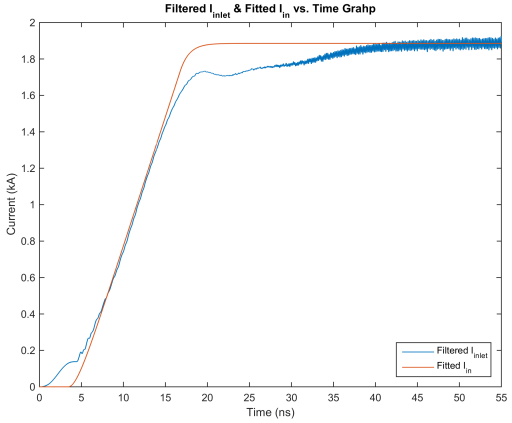
Filtered I_{inlet} & Fitted I_{in} vs. Time Grahp
Current (kA)
Time (ns)
Filtered I_{inlet}
Fitted I_{in}

(d)

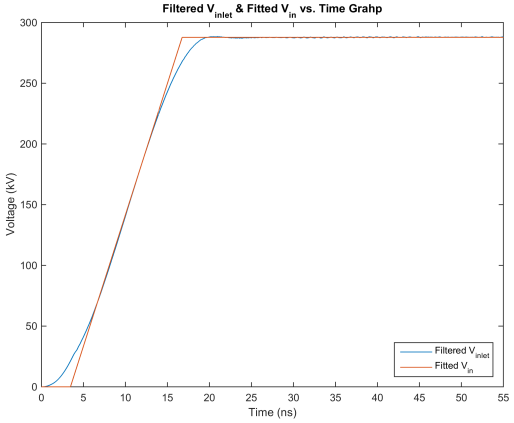
Filtered V_{inlet} & Fitted V_{in} vs. Time Grahp
Voltage (kV)
Time (ns)
Filtered V_{inlet}
Fitted V_{in}

(e)

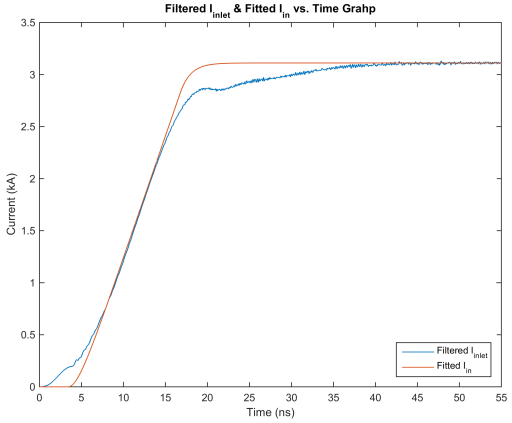
Filtered I_{inlet} & Fitted I_{in} vs. Time Grahp
Current (kA)
Time (ns)
Filtered I_{inlet}
Fitted I_{in}

(f)

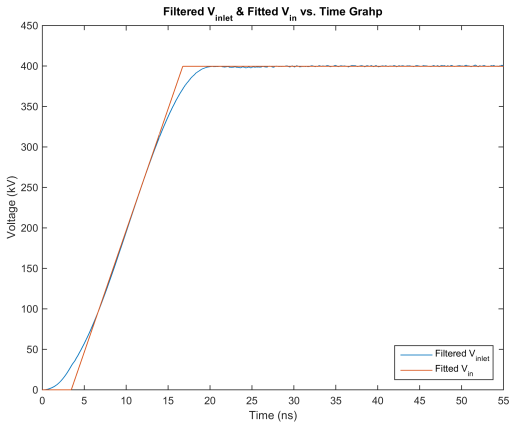

(g)

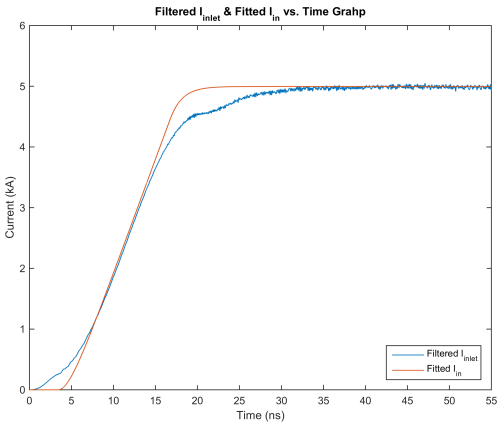

(h)

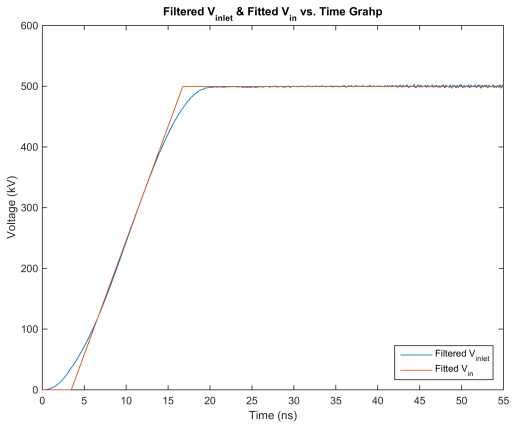

(i)

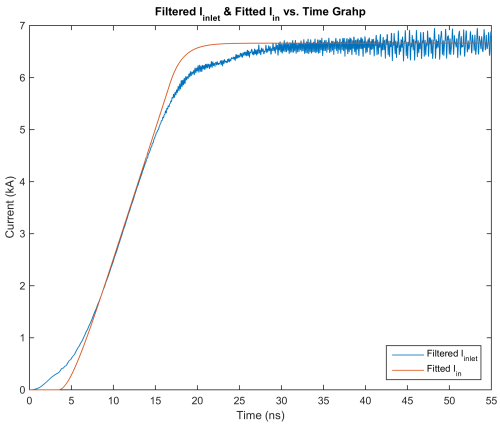

(j)

Figure A.1: Fitted (a)voltage and (b)current graphs for $V_{ak} = 100\ kV$, (c)voltage and (d)current graphs for $V_{ak} = 200\ kV$, (e)voltage and (f)current graphs for $V_{ak} = 288\ kV$, (g)voltage and (h)current graphs for $V_{ak} = 400\ kV$, (i)voltage and (j)current graphs for $V_{ak} = 500\ kV$.

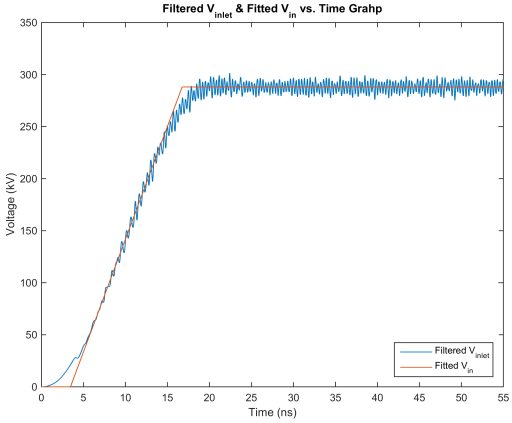
Filtered V_{inlet} & Fitted V_{in} vs. Time Grahp
Voltage (kV)
Time (ns)
Filtered V_{inlet}
Fitted V_{in}

(a)

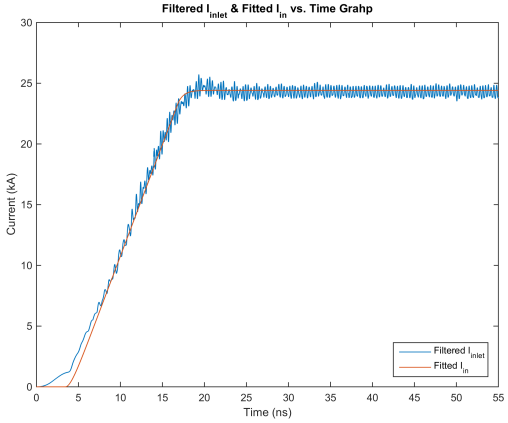
Filtered I_{inlet} & Fitted I_{in} vs. Time Grahp
Current (kA)
Time (ns)
Filtered I_{inlet}
Fitted I_{in}

(b)

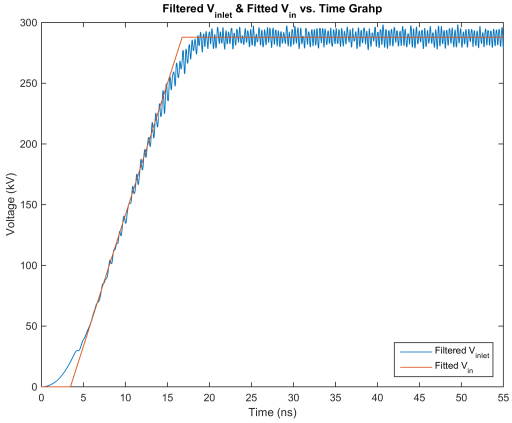
Filtered V_{inlet} & Fitted V_{in} vs. Time Grahp
Voltage (kV)
Time (ns)
Filtered V_{inlet}
Fitted V_{in}

(c)

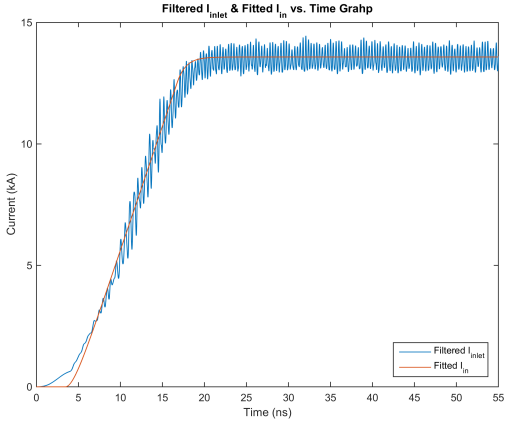
Filtered I_{inlet} & Fitted I_{in} vs. Time Grahp
Current (kA)
Time (ns)
Filtered I_{inlet}
Fitted I_{in}

(d)

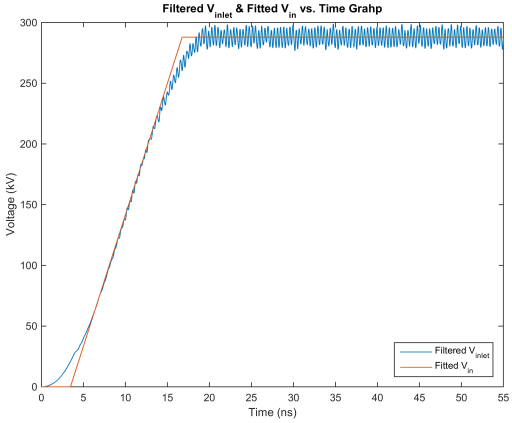
Filtered V_{inlet} & Fitted V_{in} vs. Time Grahp
Voltage (kV)
Time (ns)
Filtered V_{inlet}
Fitted V_{in}

(e)

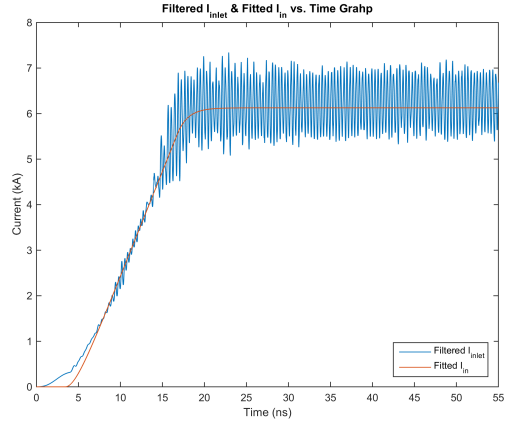
Filtered I_{inlet} & Fitted I_{in} vs. Time Grahp
Current (kA)
Time (ns)
Filtered I_{inlet}
Fitted I_{in}

(f)

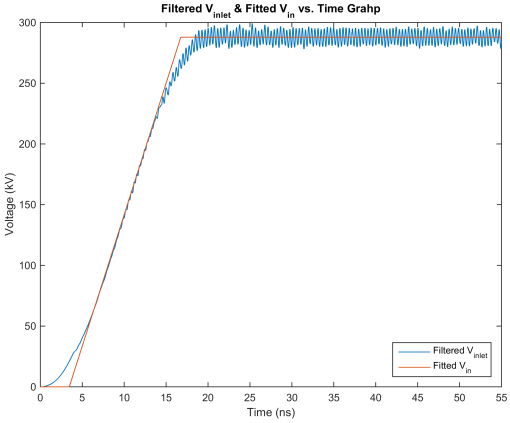
Filtered V_{inlet} & Fitted V_{in} vs. Time Grahp
Voltage (kV)
Time (ns)
Filtered V_{inlet}
Fitted V_{in}

(g)

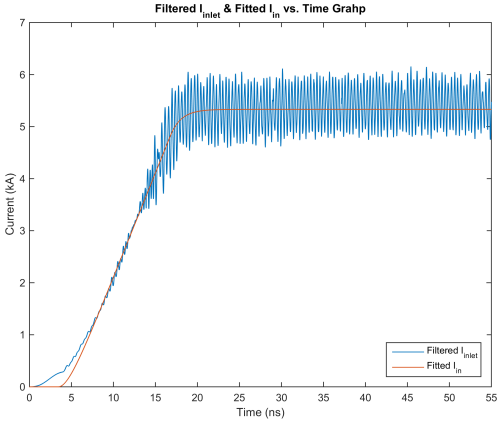
Filtered I_{inlet} & Fitted I_{in} vs. Time Grahp
Current (kA)
Time (ns)
Filtered I_{inlet}
Fitted I_{in}

(h)

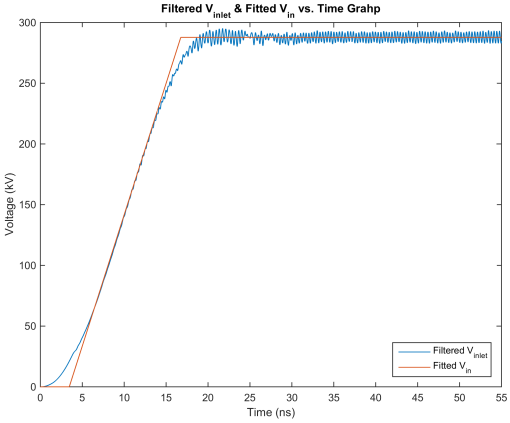
Filtered V_{inlet} & Fitted V_{in} vs. Time Grahp
Voltage (kV)
Time (ns)
Filtered V_{inlet}
Fitted V_{in}

(i)

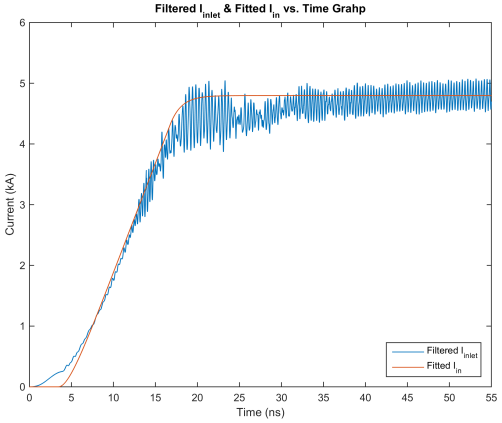
Filtered I_{inlet} & Fitted I_{in} vs. Time Grahp
Current (kA)
Time (ns)
Filtered I_{inlet}
Fitted I_{in}

(j)

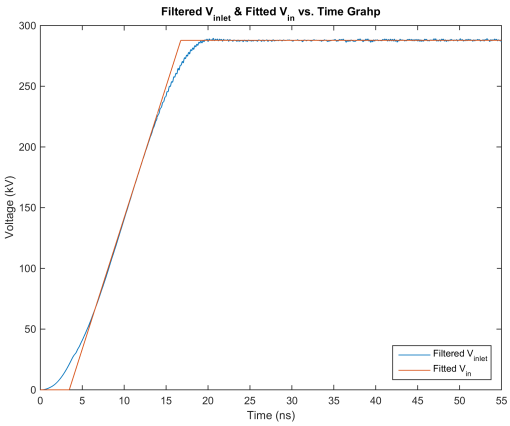
Filtered V_{inlet} & Fitted V_{in} vs. Time Grahp
Voltage (kV)
Time (ns)
Filtered V_{inlet}
Fitted V_{in}

(k)

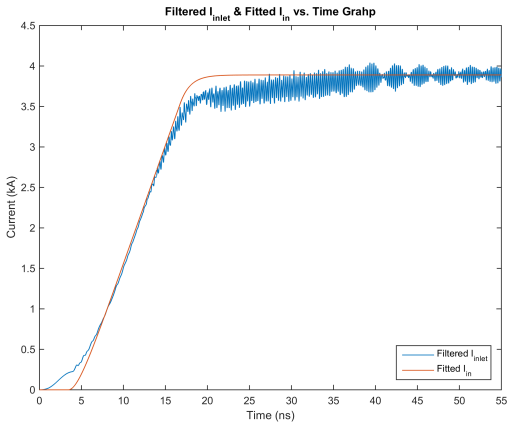
Filtered I_{inlet} & Fitted I_{in} vs. Time Grahp
Current (kA)
Time (ns)
Filtered I_{inlet}
Fitted I_{in}

(l)

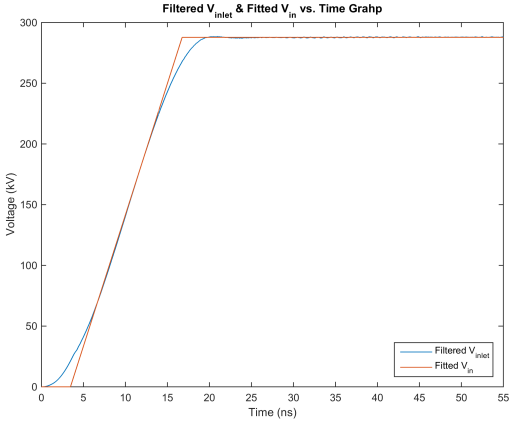

(m)

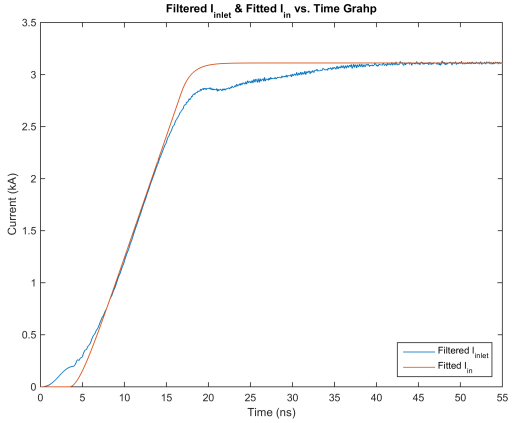

(n)

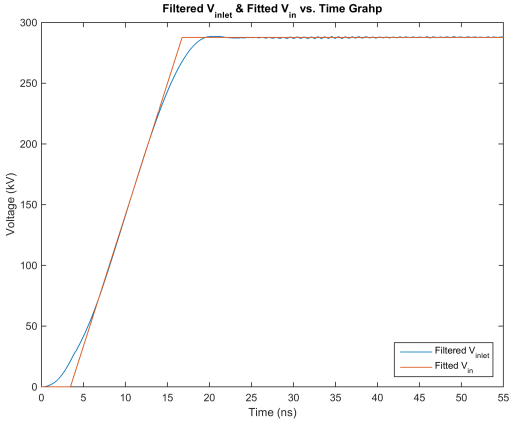

(o)

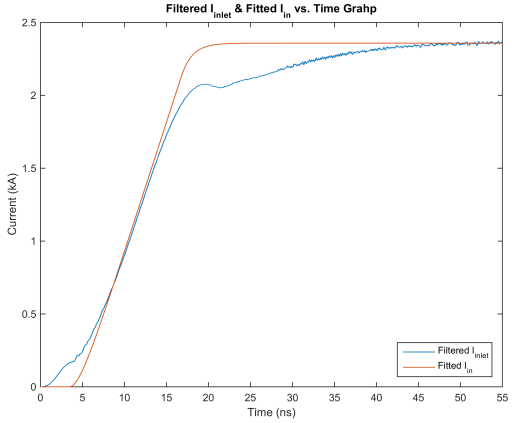

(p)

Figure A.2: Fitted (a)voltage and (b)current graphs for $r_c = 135\ mm$, (c)voltage and (d)current graphs for $r_c = 85\ mm$, (e)voltage and (f)current graphs for $r_c = 45\ mm$, (g)voltage and (h)current graphs for $r_c = 40\ mm$, (i)voltage and (j)current graphs for $r_c = 35\ mm$, (k)voltage and (l)current graphs for $r_c = 30\ mm$, (m)voltage and (n)current graphs for $r_c = 25\ mm$, (o)voltage and (p)current graphs for $r_c = 20\ mm$.

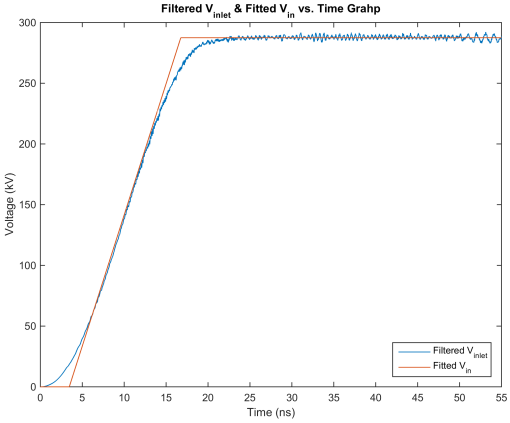
Filtered V_{inlet} & Fitted V_{in} vs. Time Grahp
Voltage (kV)
Time (ns)
Filtered V_{inlet}
Fitted V_{in}

(a)

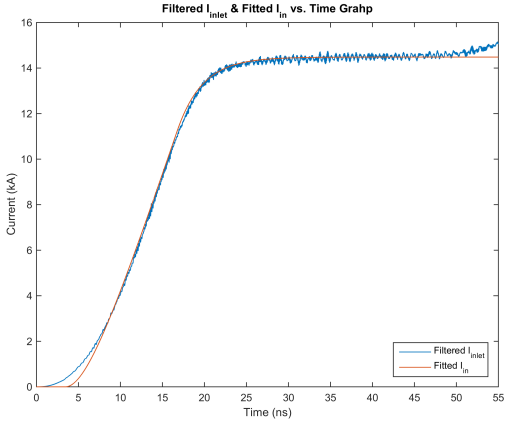
Filtered I_{inlet} & Fitted I_{in} vs. Time Grahp
Current (kA)
Time (ns)
Filtered I_{inlet}
Fitted I_{in}

(b)

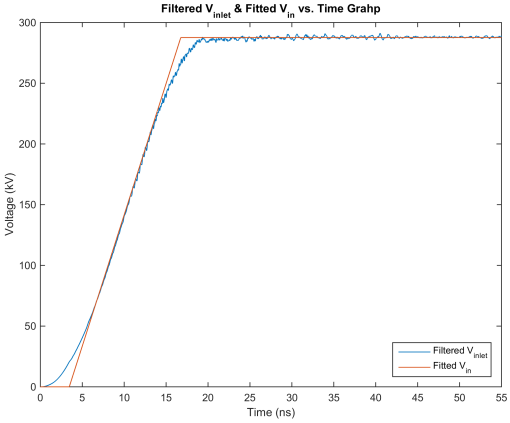
Filtered V_{inlet} & Fitted V_{in} vs. Time Grahp
Voltage (kV)
Time (ns)
Filtered V_{inlet}
Fitted V_{in}

(c)

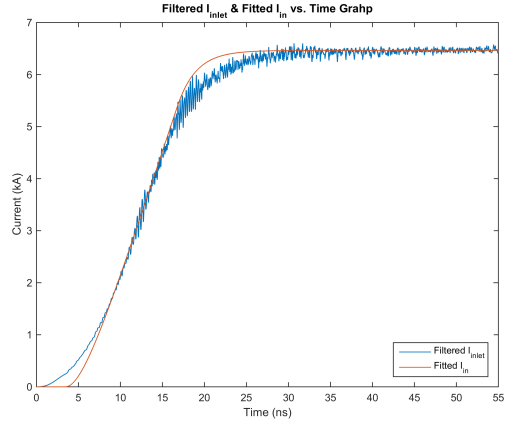
Filtered I_{inlet} & Fitted I_{in} vs. Time Grahp
Current (kA)
Time (ns)
Filtered I_{inlet}
Fitted I_{in}

(d)

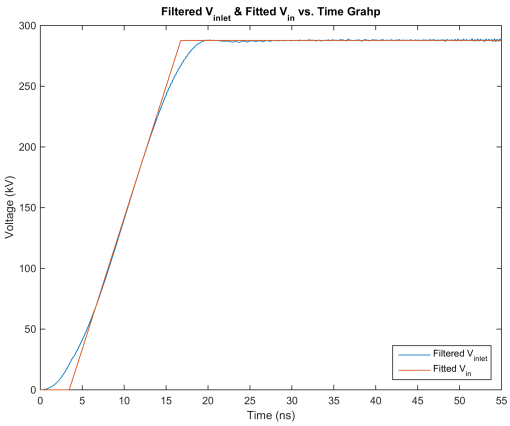
Filtered V_{inlet} & Fitted V_{in} vs. Time Grahp
Voltage (kV)
Time (ns)
Filtered V_{inlet}
Fitted V_{in}

(e)

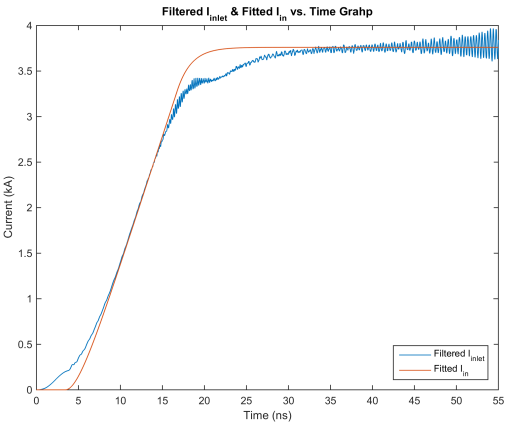
Filtered I_{inlet} & Fitted I_{in} vs. Time Grahp
Current (kA)
Time (ns)
Filtered I_{inlet}
Fitted I_{in}

(f)

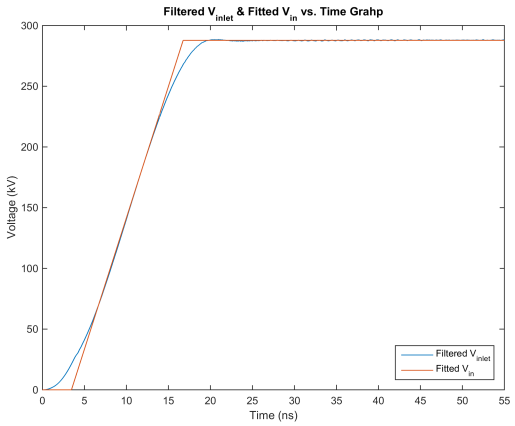

(g)

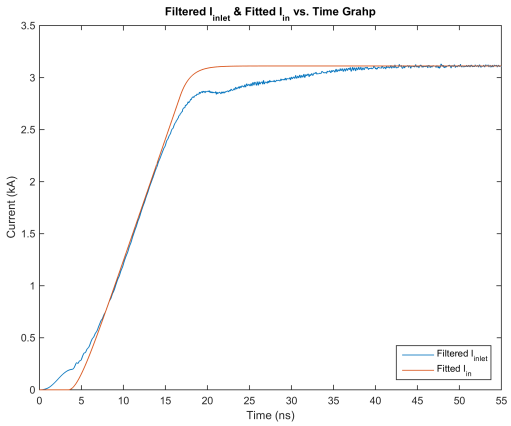

(h)

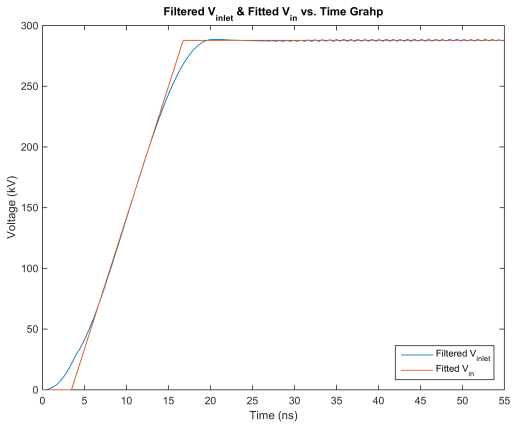

(i)

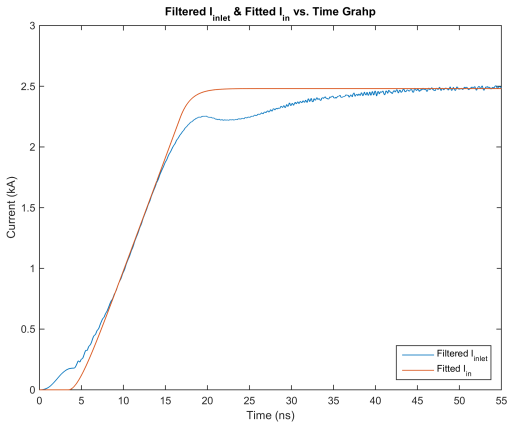

(j)

Figure A.3: Fitted (a)voltage and (b)current graphs for $d_{ak} = 5\ mm$, (c)voltage and (d)current graphs for $d_{ak} = 10\ mm$, (e)voltage and (f)current graphs for $d_{ak} = 15\ mm$, (g)voltage and (h)current graphs for $d_{ak} = 17\ mm$, (i)voltage and (j)current graphs for $d_{ak} = 20\ mm$.